THE ASTROPHYSICAL JOURNAL, 390:108–132, 1992 May 1

GALACTIC WORMS. I. CATALOG OF WORM CANDIDATES

BON-CHUL KOO[1], CARL HEILES, AND WILLIAM. T. REACH[2]
Astronomy Department, University of California, Berkeley, CA 94720
Received 1991 September 9; accepted 1991 November 5

ABSTRACT

We have found and cataloged 118 isolated structures that appear both in H I and in infrared (60 and 100 μm). In the inner Galaxy, these correspond to the "H I worms" detected by Heiles. The worms are thought to be the walls surrounding superbubbles which have broken through the thin gaseous disk inside the solar circle. Among 118 structures, 52 are possibly associated with H II regions. The structures associated with H II regions have a higher probability for association with superbubbles. Upon analysis of the catalog, we found that (1) the 100 μm emissivity, $I_{100}/N_{\rm H\,I}$, increases systematically toward the Galactic interior, which is consistent with the increase of the general interstellar radiation field, (2) the 100 μm emissivity of the structures associated with H II regions is larger than that of the structures without associated H II regions, and (3) the 60–100 μm ratio is large, 0.28 ± 0.03, which may indicate that the grains associated with atomic gas have a relatively large population of small grains. Among 118 structures, 35 appear in the 408 MHz continuum. About 70% of the 35 structures are possibly associated with H II regions. The infrared and the radio continuum properties suggest that the 408 MHz continuum emission in those structures is very likely *thermal.* The thermal emission probably originates from the gas ionized by photons from stars located in the same general region that produce the H II region. Some individual objects are briefly described. We discuss implications of our results on the ionization of gas far from the Galactic plane.

Subject headings: catalogs — H II regions — ISM: bubbles — radio continuum: interstellar — radio lines: atomic

1. INTRODUCTION

Stellar winds and supernova (SN) explosions from the OB association can produce a gigantic hot bubble surrounded by a dense shell, superbubble, and supershell. If the injected energy is large enough, the superbubbles can break through a thin gaseous galactic disk and "punch" holes in the interstellar medium. Indeed, in nearby galaxies, e.g., M31, M33, M101, the broken-through superbubbles have been observed as holes in H I gas (Allen, Goss, & van Woerden 1973; Allen et al. 1978; Brinks & Bajaja 1986; Deul & den Hartog 1990; Kamphuis, Sancisi, & van de Hulst 1991).

In our Galaxy, the detection of such structure is very difficult because of the background emission. However, if we can detect such structures in our Galaxy, then we can also obtain detailed information because of their proximity. Heiles (1984), in his pioneering study of H I shells and supershells, found interesting features in the inner Galaxy, "H I worms": By applying a median filter, which enhances small scale structure, to the H I channel maps near the Galactic plane ($|b| < 10°$), he found that the filtered structure appears to be random in the outer Galaxy, while in the inner Galaxy it tends to run perpendicular to the Galactic plane and individual features tend to persist over a large velocity interval. He interpreted these vertical structures, or H I worms, as the walls surrounding superbubbles which have broken through the thin gaseous disk inside the solar circle. Other than their morphological suggestions, however, there is no other evidence for this interpretation, mainly because no more studies have been done on these objects after Heiles's work. In this series of papers, we would like to pursue these studies.

The study of the worms has some importnat implications if they are really the walls of broken-through superbubbles. First, the study of individual worms may tell us how the superbubbles break through the thin gaseous disk and even how they blow out the thick gaseous disk. (We follow the nomenclature of Heiles [1990] who used the words "break-through" and "blow-out" to distinguish the phenomena related to the thin disk and the thick disk, respectively. As far as the phenomena do not refer to a specific disk, we used them interchangeably.) The dynamics of superbubble blow-out has been studied numerically by many authors (Tomisaka & Ikeuchi 1986; Tenorio-Tagle, Bodenheimer, & Ròżyczka 1987; Mac Low & McCray 1988; Mac Low, McCray, & Norman 1989; Tomisaka 1990), but a detailed comparison with real objects could not be made because of the lack of observations. The high-resolution observations of individual worms at multifrequencies will provide invaluable information for the study of superbubble blowout phenomena. Second, the distribution of the worms in the Galaxy may tell us about the filling factor of the hot ionized gas. If the worms are really the walls surrounding superbubbles which are filled with hot gas, then the distribution of the worms in the Galaxy should be directly related to the filling factor of the hot ionized gas.

In this paper, we present the catalog of 118 "worm candidates" and study their statistical properties. Preliminary results have been presented by Koo, Heiles, & Reach (1990). Individual candidates will be studied in subsequent papers. The 118 structures are found and cataloged by an *unbiased* technique using the H I 21 cm map, and *IRAS* 100 and 60 μm maps. We call them worm candidates because, if we define the worms as *the structures perpendicular to the Galactic plane*

---

[1] Also Harvard-Smithsonian Center for Astrophysics, 60 Garden Street, Cambridge, MA 02138.

[2] Current address: NASA Goddard Space Flight Center, Code 685, Greenbelt, MD 20771.

regardless of their origin, many (about $\frac{2}{3}$) of candidates do not satisfy this morphological definition. However, as will be seen later in this paper, they can be used to derive some global properties of our Galaxy. We also searched for the similar structures in 408 MHz radio continuum emission. Among 118 objects, we have found that 35 have a corresponding structure. In § 2 we summarize the data base and how we search for the worm candidates. The catalog of 118 structures and also the catalog of 35 structures that appear in radio continuum are given in § 3. Some basic statistical properties of these objects are studied in § 4.1. By cross-correlating the catalog of worm candidates with the catalogs of known H II regions, we have found that 52 structures possibly have an associated H II region. The list of those 52 structures is given in § 4.2. The correlations among various physical properties are examined in § 4.3. Some individual candidates of particular interest are briefly described in § 5. The implications of our results are discussed in § 6, and, finally, in § 7 we summarize our results.

2. OBSERVATIONS AND DATA ANALYSIS

2.1. *Observations and Data*

We made H I 21 cm maps of the Galactic plane ($|b| < 10°$) from both available surveys and a new observation. Between $l = 10°$ and 350°, we used the Galactic plane survey of Weaver & Williams (1973) and of Kerr et al. (1986). The Weaver-Williams survey was done by stepping through in Galactic latitude at a given Galactic longitude. The beam spacing was 0°.5 in longitude and 0°.25 in latitude. The Kerr et al. survey has been done by drift-scanning through in right ascension at a given declination. The beam spacing was 0°.33 in right ascension and 0°.5 in declination. The coverage in Galactic longitude, beam size, velocity coverage, velocity resolution, and the sensitivity of the two surveys are listed in Table 1 (see Burton 1988). From overlapping regions, we found that the antenna temperature scale in the two surveys is related by WW/Kerr = 0.84 ± 0.06, which is consistent with 0.85 ± 0.01 obtained by Kerr et al. We used the main beam efficiency of 0.8 to convert the observed antenna temperature of the Weaver-Williams survey to the brightness temperature, and 1.0 for the Kerr survey.

We obtained the H I data near the Galactic center ($350° \leq l \leq 10°$; $|b| \leq 10°$) during 1989 and 1990 using the Hat Creek 85 foot (26 m) telescope. The observations were made on the Galactic longitude-latitude grid at half-degree spacing. The area below $\delta = -40°$, which occupies ~4% of the mapping area, was unreachable by the Hat Creek telescope. Both circular polarizations were observed simultaneously with two 512 channel correlators, each with a total bandwidth of 5 MHz. Spectra were obtained by frequency switching to higher frequencies of 5 MHz and by integrating for 240 s (ON + OFF). The observing parameters are listed in Table 1. Again, we used the main beam efficiency of 0.8 to convert the observed antenna temperature to the brightness temperature.

We created the infrared 100 and 60 μm maps of the Galactic plane from the *IRAS* Zodiacal Observation History File (1988), which contains the time-ordered list of infrared sky brightness observations. The outputs of all detectors in the *IRAS* focal plane were averaged together (separately in each of the four wavebands), and the data were smoothed in time, in order that the effective resolution is 0°.5. We created our all-sky maps using only *IRAS* scans made with solar elongations between 80° and 100°, so that the contribution to the infrared background by the zodiacal emission was smooth. There are two strips on opposite sides of the sky, each ~5° wide and 60° long, that are not observed (*IRAS* Explanatory Supplement 1988). Near the Galactic plane, they are located at $l = 85°$ and 265°, and their widths are less than 3° and 2°, respectively. The unobserved area occupies 0.9% of the total area between $b = -10°$ and $+10°$.

For the radio continuum map of the Galactic plane, we used the 408 MHz survey of Haslam et al. (1982). The survey was done using different telescopes with beam sizes ranging from 37′ to 51′. According to Haslam et al., the temperature scale is accurate to better than 10%, while the average zero level has an uncertainty of ±3 K.

All the maps have a pixel size of 0°.5 × 0°.5. The pixels without data (see above) are interpolated to the inverse square law. A major problem in these surveys is the so-called "stripes," which appear along scan directions due to either incomplete baseline removal or calibration errors. The stripes are most apparent in the H I map between $l = 250°$ and 350° (see Figure 1 below). We found that the rms fluctuation in the H I column density between the scans is $\sim 5 \times 10^{19}$ cm^{-2}, which is smaller than the average column density of the cataloged structures but is not negligible (~25%; see Table 3). The *IRAS* maps also have stripes. According to Désert, Bazell, & Boulanger (1988), the rms fluctuation is ~0.5 MJy sr^{-1} at 100 μm, which is ~15% of the average 100 μm surface brightness of the cataloged structures. In this study, we have not tried to remove these stripes. Our study is based on the correlation at different frequencies, and the stripes, which appear at different directions at different frequencies, are very unlikely to produce a correlated structure. However, it increases the error in the surface brightness of correlated structures, which might be greater than 30%.

TABLE 1

OBSERVATIONAL PARAMETERS OF H I SURVEYS

Longitude	H I Survey Reference[a]	Beam	v-Coverage (km s^{-1})	v-Resolution (km s^{-1})	Sensitivity (K)
10°–250°	1	36′	$v_0 \pm 125$[b]	2.1 (6.3)[c]	0.4 (0.2)[c]
240 –350	2	48	$v_0 \pm 117$	2.1	0.3
350 –10	3	36	± 528	4.1[d]	0.09[d]

[a]—(1) Weaver & Willers 1973; (2) Kerr et al. 1986; (3) this paper.

[b] Between $l = 10°$ and 14° and $b = -4°$ and $+4°$, they also obtained profiles between $v_{\rm LSR} = +120$ km s^{-1} and $+240$ km s^{-1}. This data set has not been included in our analysis.

[c] The velocity-resolution and the sensitivity values in parenthesis refer to end points of the profile.

[d] After Hanning smoothing.

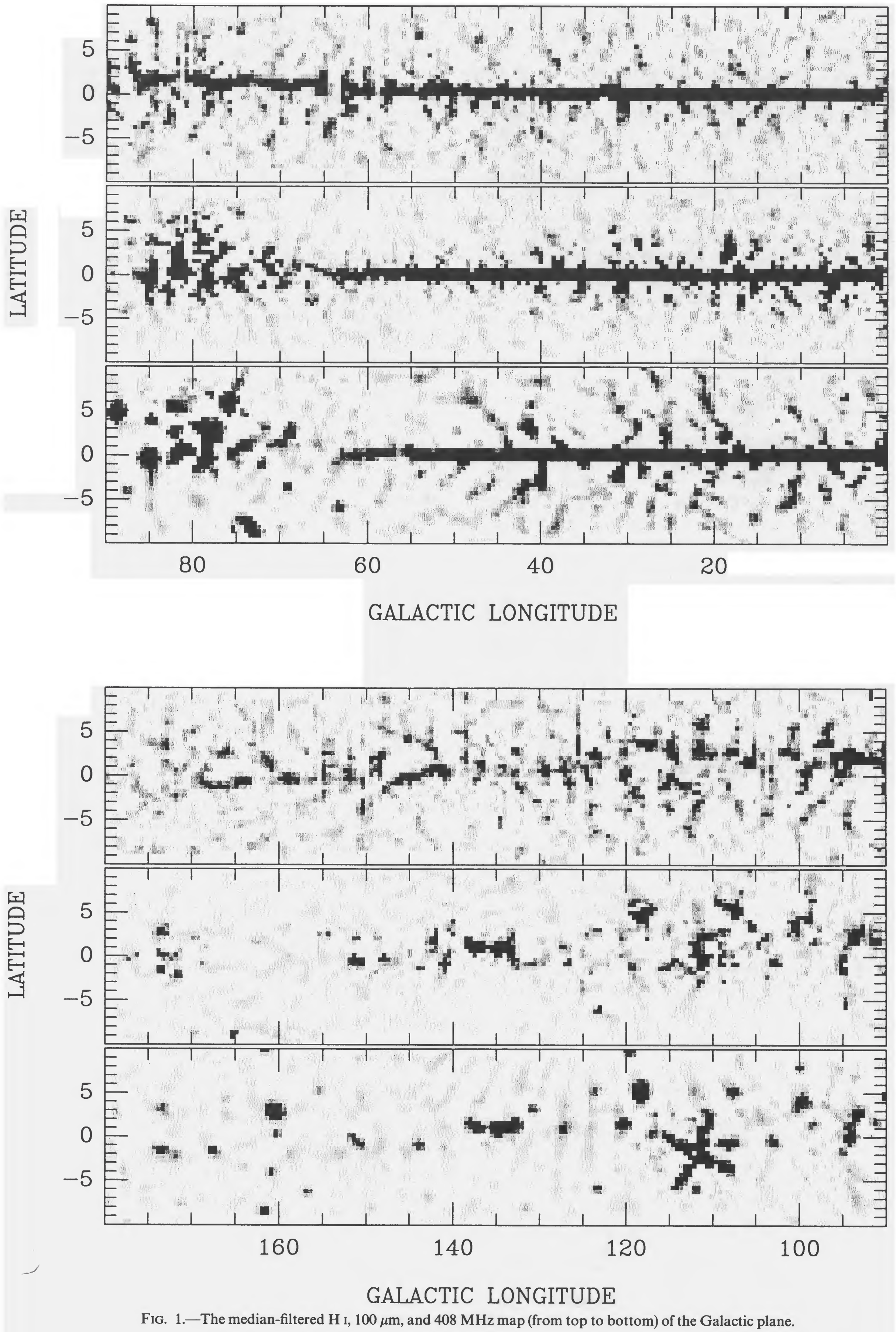

FIG. 1.—The median-filtered H I, 100 μm, and 408 MHz map (from top to bottom) of the Galactic plane.

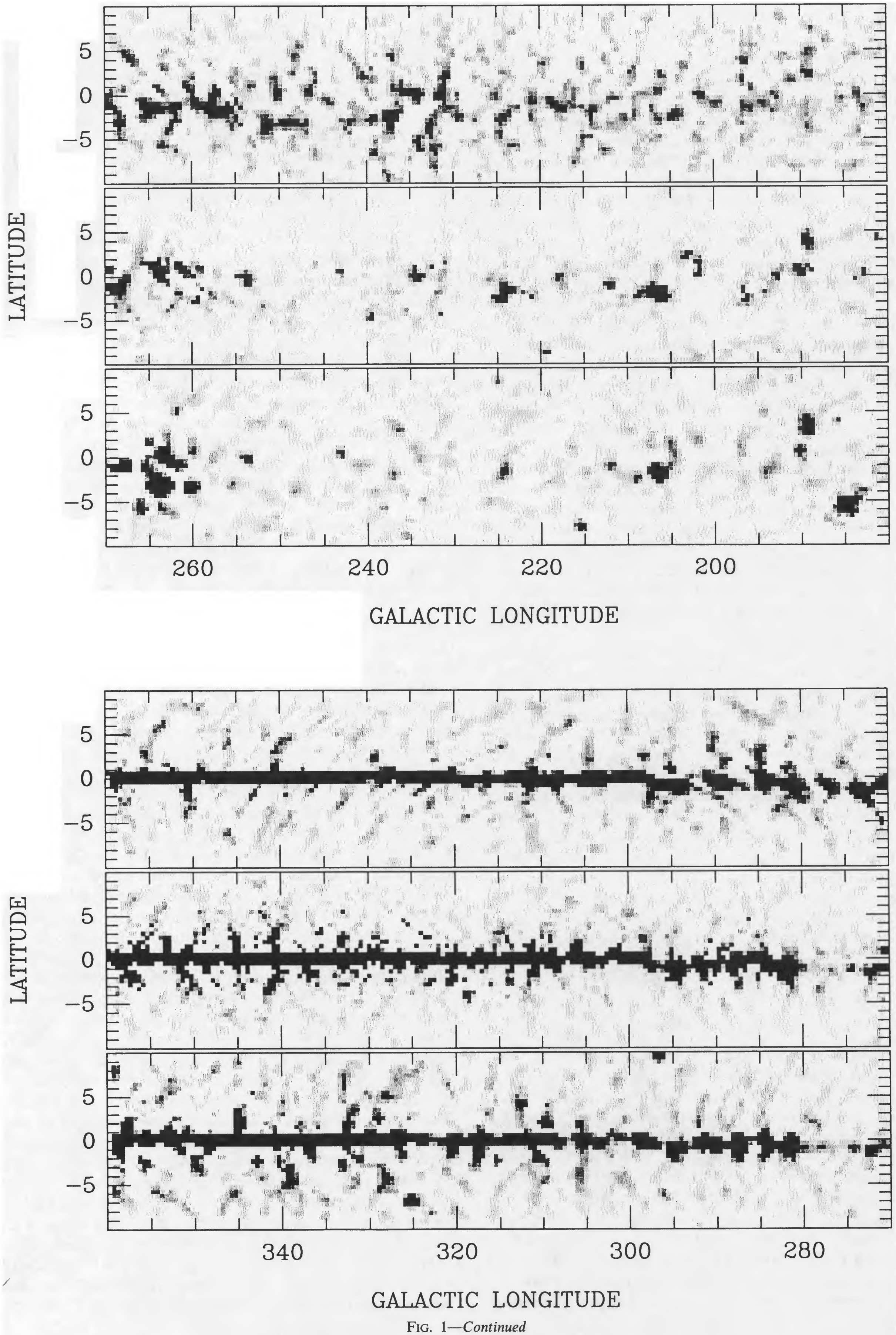

FIG. 1—*Continued*

2.2. *Data Analysis*

We first applied a median filter of 3°.5 × 3°.5 to the H I map integrated between $v_{\rm LSR} = -200$ and $+200$ km s^{-1} (see note in Table 1), the 100 μm map, the 60 μm map, and the 408 MHz map. The median filtering is to subtract the median value of the surrounding pixels (48 pixels in our case) from a given pixel, and it enhances structures smaller than the filter size. Figure 1 shows the median-filtered H I map together with the corresponding 100 μm and 408 MHz maps. In Figure 1, several thing are to be noted. First we can see the Galactic plane near $b = 0°$. The Galactic plane outside the solar circle is warped in the sense that the plane defined by the maximum density of the H I gas layer is significantly above $b = 0°$ between $l = 0°$ and 180° and is slightly below $b = 0°$ between $l = 180°$ and 360° (see Burton 1988). This is clearly seen in the median-filtered H I map, which integrates all the emission including that from the warped out Galactic plane. On the other hand, the warped Galactic plane in the first quadrant is not seen in the other maps, because they are strongly weighted by the emission in the inner Galaxy. In the case of the 100 μm emission, the emissivity increases toward the inner Galaxy due to the increase of the interstellar radiation field (Mathis, Mezger, & Panagia 1983; see also § 4), whereas in the case of the 408 MHz emission, the emissivity increases toward the inner Galaxy due to the increase of sources, e.g., supernova remnant and H II regions (Beuermann, & Berkhuijsen 1985). Second, we can see vertical structures rising from the Galactic plane in the inner Galaxy, which are the worms. There is a detailed correlation between the H I and the 100 μm map, which proves that most of these structures are real.

In the median-filtered maps, an isolated structure is identified by an "unbiased" computer algorithm, which searches for pixels with positive values and connected with each other. (For a given pixel, we consider only four nearest-neighbor pixels.) The central region of the plane $(-1° < b < +1°)$ is excluded because those pixels have all positive values in the inner Galaxy. If the total number of connected pixels is greater than or equal to 5, we consider those connected pixels as a structure. We have identified a total of 342, 376, 409, and 359 structures in H I, 100 μm, 60 μm, and 408 MHz maps, respectively. The number of structures in the upper $(b > 0)$ region is comparable to that in the lower $(b < 0)$ region.

The correlated structures at different wavelengths are identified in the following way. We define a cross-correlation parameter $r(A, B)$ of two structures A and B at different wavelengths by

$$r(A, B) = \frac{\text{area } (A \cap B)}{\sqrt{\text{area } (A) \times \text{area } (B)}}\,, \tag{1}$$

where area (A) and area (B) are the areas occupied by the structure A and B, respectively, and area $(A \cap B)$ is the area occupied by both A and B. We assume that two structures are correlated if r is greater than 0.5. By cross-correlating the H I, 100 μm, and 60 μm maps, we have found 118 structures that appear in both H I and infrared maps, i.e., with r greater than 0.5 in two of the three (H I 100 μm, H I 60 μm, and 100–60 μm) cross-correlations. The finding chart of 118 structures is given in Figure 2, where a number is assigned to each structure in an increasing order of l. In Figure 2, each structure is marked by blackening the total area, *area* (H I ∪ 100 μm ∪ 60 μm), and therefore the structures with different identification number can look as if they are connected. A noticeable thing in Figure 2 is the lack of correlated structures in the upper region between $l = 80°$ and 180°, and in the lower region between $l = 180°$ and 280°. This is because the Galactic plane is warped and the excluded the central region of the plane $(-1° < b < +1°)$. In other words, in those regions where the Galactic plane is considerably warped, most pixels with positive values are connected and two structures in different wavebands rarely have $r > 0.5$. We will call 118 structures "worm candidates" even though some of them are small and at high latitudes, so that they are certainly not the worms in the sense that they do not "crawl out of the Galactic plane."

We determined the velocity of each structure by cross-correlating the final map (Fig. 2) with H I channel maps integrated over 4 km s^{-1}. The cross correlation with H I channel maps is somewhat different from the above, because a structure generally persists over a large velocity interval, and we want to know the velocity center and the minimum velocity. We first identified isolated structures in each median-filtered channel map and then cross-correlated Figure 2 with each channel map. At a given velocity, we computed the cross-correlation coefficient r and the column density of each structure in Figure 2. We plotted the column density weighted by a cross-correlation coefficient for each structure as a function of velocities. For most worm candidates, the plot showed a well-defined peak, in which case we fitted a Gaussian to obtain the central velocity and velocity dispersion. For some structures, however, the plot showed double peaks, or even multiple peaks. In this case, we determined the velocity in the following way. First, if the cross-correlation coefficient at one peak was considerably larger than others, then we took the velocity of that peak. Second, if the peaks were close to each other, we fitted a wide Gaussian. Otherwise, we took the velocity of the peak corresponding to a closer distance.

We also cross-correlated the final map (Fig. 2) with the median-filtered 408 MHz map. Among 118 structures, 35 have counterparts at 408 MHz.

3. CATALOG OF WORM CANDIDATES

Some physical properties of 118 structures are listed in Table 2. Column (1) contains the running number, which can be used to locate the structure in Figure 2. Column (2) contains the name, which specifies the longitude and latitude of the center of the structure. The central position is determined by averaging the positions of all pixels in the structure in three wavebands. Columns (3) and (4) contain the angular sizes in longitude and latitude, respectively. Columns (5) and (6) contain the minimum and the maximum velocities determined at the half-maximum of the Gaussian fitting, respectively. The velocities of those structures with double or multiple peaks are listed with a question mark. Column (7) contains the Galactocentric radius, calculated assuming $R_\odot = 8.5$ kpc and a flat rotation curve with $v_\odot = 220$ km s^{-1}. The velocities of some structures are fobidden by the flat Galactic rotation model, and for these the Galactocentric radius could not be determined. The Galactocentric radii of those structures with uncertain velocities are listed with question marks, as also for the other distance-dependent physical parameters. Column (8) contains the distance to these objects. For structures in the inner Galaxy, we always take the "near" distance. With our method in this paper, it is hard to detect structures on the other side of the Galaxy unless they are very large (see § 4.1; see also some possible exceptions in § 5). Columns (9) and (10) contain the minimum and the maximum heights above the Galactic plane.

TABLE 2.—*Continued*

										H I Properties			Infrared Properties					
Number (1)	Name (2)	Δl (deg) (3)	Δb (deg) (4)	$v_{\rm min}$ (km s^{-1}) (5)	$v_{\rm max}$ (km s^{-1}) (6)	R_G (kpc) (7)	d (kpc) (8)	$z_{\rm min}$ (pc) (9)	$z_{\rm max}$ (pc) (10)	Area (deg^2) (11)	$\bar{N}_{\rm H\,I}$ (cm^{-2}) (12)	$M_{\rm H\,I}$ ($M_\odot$) (13)	Area (deg^2) (14)	r (15)	$\bar{I}_{100}$ (MJy sr^{-1}) (16)	$\bar{I}_{60}$ (MJy sr^{-1}) (17)	I_{60}/I_{100} (18)	$I_{100}/N_{\rm H\,I}$ (MJy sr^{-1}/10^{20} cm^{-2}) (19)
64	GW 175.8−2.5	13.0	4.5	−30.6	3.6	...	...	...	...	16.0	1.7 ± 6.1	...	22.0	0.45	6.2 ± 9.8	3.8 ± 6.1	0.33 ± 0.41	3.2 ± 13
65	GW 177.3+1.4	3.0	1.0	−21.8	−12.1	...	...	...	...	2.0	1.8 ± 0.4	...	2.0	0.50	2.1 ± 0.8	0.9 ± 0.4	0.35 ± 0.12	0.6 ± 0.7
66	GW 192.0+8.7	2.5	3.0	−10.1	−2.1	...	...	...	...	2.5	1.8 ± 0.3	...	3.8	0.82	1.8 ± 1.0	0.4 ± 0.3	0.29 ± 0.54	1.3 ± 2.9
67	GW 193.8+2.7	1.0	1.5	−2.9	17.4	9.9	1.4	50	80	1.5	0.9 ± 0.2	0.64E+03	1.5	0.67	1.4 ± 0.9	0.3 ± 0.2	0.33 ± 0.24	1.8 ± 10
68	GW 195.7+4.5	5.5	6.5	11.7	32.8	13.6	5.2	90	680	14.0	2.1 ± 0.2	0.19E+06	9.3	0.53	1.5 ± 1.4	0.5 ± 0.2	0.25 ± 0.33	0.9 ± 1.7
69	GW 211.5+6.9	5.0	7.5	3.2	20.2	9.5	1.1	50	200	10.0	1.4 ± 0.2	0.41E+04	4.8	0.51	1.6 ± 1.3	0.3 ± 0.2	0.10 ± 1.65	1.1 ± 11
70	GW 213.4+1.4	2.0	1.0	36.5	44.4	12.8	4.8	80	170	2.3	1.4 ± 0.3	0.17E+05	1.8	0.63	2.2 ± 0.9	0.5 ± 0.3	0.15 ± 0.09	1.2 ± 23
71	GW 216.6+1.3	2.5	1.0	18.0	51.1	11.6	3.5	60	120	1.5	1.8 ± 0.8	0.81E+04	2.0	0.58	3.4 ± 2.9	0.9 ± 0.8	0.26 ± 0.16	2.1 ± 10
72	GW 220.0+3.6	3.0	5.0	53.3	60.7	14.2	6.6	120	700	5.0	2.2 ± 0.1	0.12E+06	5.0	0.40	0.8 ± 0.7	0.2 ± 0.1	0.25 ± 0.36	0.2 ± 0.3
73	GW 230.8+5.2	6.5	8.5	14.9	41.5	10.2	2.4	40	400	18.0	2.0 ± 0.9	0.50E+05	21.0	0.73	1.9 ± 4.0	0.7 ± 0.9	0.27 ± 0.39	0.6 ± 5.9
74	GW 239.2+7.4	4.5	6.5	56.7?	86.9?	13.7?	7.3?	440?	1280?	9.0	0.8 ± 0.1	0.96E+05	5.5	0.57	0.6 ± 0.3	0.3 ± 0.1	0.40 ± 0.37	1.3 ± 3.6
75	GW 239.9+3.4	7.5	5.5	36.5	76.1	12.1	5.3	90	600	10.0	2.4 ± 0.4	0.17E+06	12.0	0.83	1.3 ± 1.2	0.4 ± 0.4	0.22 ± 0.19	0.7 ± 1.8
76	GW 243.9+2.1	1.5	2.5	18.0	26.0	9.6	2.0	40	120	1.8	1.1 ± 0.7	0.19E+04	3.3	0.63	1.5 ± 1.4	0.6 ± 0.7	0.20 ± 0.33	1.0 ± 0.9
77	GW 247.9+4.6	3.5	8.0	7.0?	20.1?	9.1?	1.4?	20?	220?	11.0	1.9 ± 0.1	0.95E+04	12.0	0.71	1.0 ± 0.6	0.3 ± 0.1	0.19 ± 0.14	0.5 ± 0.2
78	GW 250.6+2.0	2.0	2.5	17.6?	25.5?	9.5?	2.3?	40?	140?	4.3	2.5 ± 0.1	0.13E+05	2.5	0.69	0.8 ± 0.5	0.2 ± 0.1	0.25 ± 0.20	0.2 ± 0.5
79	GW 253.9+2.6	4.5	3.5	30.8	58.2	10.8	4.7	80	370	6.3	2.2 ± 0.2	0.73E+05	4.8	0.46	1.4 ± 0.9	0.3 ± 0.2	0.24 ± 0.29	0.6 ± 0.6
80	GW 257.5+8.1	7.5	4.5	3.4	7.6	8.7	0.9	80	150	3.3	1.0 ± 0.3	0.58E+03	7.8	0.55	1.3 ± 1.0	0.3 ± 0.3	0.23 ± 0.54	2.6 ± 3.3
81	GW 257.9+4.1	2.0	2.5	18.0	22.0	9.4	2.5	130	250	1.5	1.4 ± 0.4	0.33E+04	3.5	0.65	1.6 ± 1.0	0.5 ± 0.4	0.23 ± 0.15	0.9 ± 1.4
82	GW 260.9+6.1	3.0	3.5	14.3?	32.7?	9.5?	3.2?	220?	420?	4.8	1.1 ± 0.3	0.13E+05	5.3	0.55	1.4 ± 0.8	0.5 ± 0.3	0.35 ± 0.18	1.9 ± 1.5
83	GW 261.9−9.6	3.5	1.5	71.0?	81.0?	13.1?	8.8?	−1550?	−1310?	1.3	1.0 ± 0.6	0.23E+05	1.3	1.00	2.2 ± 1.1	0.4 ± 0.6	0.31 ± 0.51	2.7 ± 2.3
84	GW 271.2+8.9	4.5	2.0	13.8	19.2	9.2	3.7	520	650	6.3	1.1 ± 0.3	0.22E+05	3.8	0.77	1.8 ± 1.3	0.5 ± 0.3	0.27 ± 0.24	1.4 ± 0.8
85	GW 274.7+2.7	3.0	4.0	31.2	45.4	10.3	6.6	110	570	7.0	1.8 ± 0.2	0.13E+06	2.8	0.51	2.5 ± 2.3	0.7 ± 0.2	0.22 ± 0.07	0.7 ± 2.3
86	GW 276.5+8.5	3.0	3.0	−6.1	−2.1	...	...	...	...	2.0	0.6 ± 0.2	...	5.5	0.60	0.8 ± 0.6	0.3 ± 0.2	0.29 ± 0.27	2.2 ± 2.7
87	GW 281.5+1.5	2.0	1.0	40.5?	51.5?	10.8?	8.6?	150?	300?	1.5	5.0 ± 1.0	0.13E+06	2.8	0.62	6.2 ± 4.9	2.0 ± 1.0	0.13 ± 0.09	2.2 ± 1.1
88	GW 289.0−6.6	3.5	4.5	−35.6	−10.3	...	...	...	...	7.0	1.2 ± 0.9	...	5.0	0.59	3.9 ± 3.5	1.3 ± 0.9	0.25 ± 0.37	2.5 ± 2.8
89	GW 294.2+5.1	4.0	8.0	−40.7?	−11.2?	...	...	...	...	12.0	1.8 ± 0.8	...	12.0	0.71	4.4 ± 4.3	1.9 ± 0.8	0.25 ± 0.14	2.1 ± 4.5
90	GW 296.0−7.6	2.5	4.0	−3.6	6.0	8.6	7.6	−1330	−800	3.8	1.0 ± 0.5	0.55E+05	6.0	0.58	1.5 ± 1.2	0.5 ± 0.5	0.31 ± 0.16	1.9 ± 13
91	GW 297.8+2.6	3.0	3.5	−39.1?	−11.4?	7.5?	3.8?	70?	290?	3.3	3.2 ± 3.8	0.36E+05	6.5	0.71	11 ± 7.6	3.6 ± 3.8	0.27 ± 0.19	6.4 ± 3.4
92	GW 299.5−6.0	1.5	3.0	−19.3	−17.2	7.8	1.9	−240	−150	4.8	1.1 ± 0.3	0.44E+04	3.3	0.83	1.8 ± 1.3	0.4 ± 0.3	0.29 ± 0.26	1.6 ± 1.4
93	GW 300.4+6.2	6.5	5.5	−30.4	−9.2	7.7	2.0	120	310	13.0	1.0 ± 0.9	0.13E+05	11.0	0.67	4.0 ± 4.3	1.2 ± 0.9	0.21 ± 0.14	2.3 ± 4.2
94	GW 303.2−3.1	4.5	5.0	−3.9	46.0	9.6	11.1	−1160	−190	6.8	3.9 ± 8.8	0.78E+06	5.8	0.68	14 ± 18	7.0 ± 8.8	0.35 ± 0.69	4.1 ± 2.3
95	GW 304.6−7.8	6.0	3.5	−4.9?	13.9?	8.7?	10.0?	−1680?	−1040?	7.5	0.8 ± 0.4	0.15E+06	5.5	0.54	2.1 ± 1.8	0.6 ± 0.4	0.27 ± 0.29	1.3 ± 3.2
96	GW 305.5+9.4	4.0	1.5	−14.0	−10.0	8.0	1.0	150	170	6.0	1.1 ± 0.3	0.16E+04	3.8	0.79	2.3 ± 1.6	0.6 ± 0.3	0.28 ± 0.42	1.8 ± 14
97	GW 308.8+4.2	6.5	6.5	−57.8	−16.1	7.0	3.1	50	410	14.0	2.1 ± 1.4	0.67E+05	13.0	0.67	11 ± 17	1.8 ± 1.4	0.22 ± 0.20	3.5 ± 9.2
98	GW 310.3−4.7	8.0	8.0	−61.7?	−6.7?	7.1?	2.7?	−430?	−50?	25.0	3.4 ± 5.2	0.15E+06	16.0	0.60	13 ± 27	4.0 ± 5.2	0.25 ± 0.26	3.0 ± 5.4
99	GW 310.4+7.8	3.0	3.5	−43.2	−25.7	7.1	2.7	290	460	6.5	1.3 ± 0.5	0.15E+05	4.8	0.72	3.2 ± 1.8	0.8 ± 0.5	0.24 ± 0.28	1.9 ± 6.4
100	GW 318.0−4.1	4.0	3.5	−10.2	−4.1	8.1	0.5	−60	−20	4.8	1.5 ± 4.6	0.51E+03	3.8	0.53	17 ± 21	5.1 ± 4.6	0.29 ± 0.16	11 ± 24
101	GW 322.0+5.7	2.5	7.5	−71.6?	−45.0?	5.9?	3.9?	100?	620?	9.0	1.3 ± 0.2	0.43E+0.5	6.8	0.61	2.1 ± 1.9	0.5 ± 0.2	0.36 ± 1.89	1.7 ± 2.2
102	GW 323.0−3.1	1.5	2.0	−47.3?	−40.2?	6.4?	3.0?	−210?	−100?	2.8	2.4 ± 4.4	0.14E+05	2.8	0.82	13 ± 12	4.0 ± 4.4	0.33 ± 0.12	4.6 ± 9.0
103	GW 324.0−1.4	2.0	1.0	−70.4	−50.1	5.8	3.9	−140	−70	2.0	6.2 ± 12	0.47E+05	1.5	0.58	44 ± 38	13 ± 12	0.20 ± 0.15	2.0 ± 11
104	GW 325.2−4.3	1.5	1.5	−46.8	−31.0	6.5	2.7	−230	−160	2.8	1.1 ± 0.5	0.52E+04	1.5	0.62	4.2 ± 4.0	1.5 ± 0.5	0.39 ± 0.24	2.9 ± 4.9
105	GW 328.7−7.0	5.0	6.0	−21.4	8.0	8.0	0.6	−100	−40	9.3	1.3 ± 1.0	0.91E+03	11.0	0.64	3.9 ± 2.7	1.3 ± 1.0	0.26 ± 0.24	2.7 ± 5.4
106	GW 331.3−4.3	1.5	3.5	−106.3	−82.5	4.5	5.6	−580	−240	2.0	0.6 ± 2.5	0.85E+04	3.8	0.46	7.5 ± 6.1	2.6 ± 2.5	0.28 ± 0.09	13 ± 19
107	GW 335.6+8.2	3.5	3.5	−20.4	−14.9	7.1	1.5	180	270	4.0	0.6 ± 0.8	0.15E+04	3.8	0.58	3.0 ± 2.0	0.7 ± 0.8	0.27 ± 0.14	3.6 ± 1.6
108	GW 336.5−2.0	2.0	2.5	−130.4	−79.8	3.9	5.9	−360	−100	1.5	3.8 ± 140	0.48E+05	3.8	0.42	110 ± 140	51 ± 140	0.26 ± 0.22	61 ± 48
109	GW 340.0+4.8	4.5	8.5	−63.0?	7.6?	6.2?	2.5?	40?	420	8.3	3.5 ± 10	0.44E+05	11.0	0.59	24 ± 27	5.3 ± 10	0.25 ± 0.24	6.6 ± 6.6
110	GW 342.5+6.4	3.5	5.5	−40.0?	14.4?	7.1?	1.5?	100?	240	3.3	1.5 ± 2.9	0.24E+04	5.5	0.53	8.7 ± 7.0	1.8 ± 2.9	0.28 ± 1.17	7.5 ± 6.3
111	GW 344.9−2.8	1.5	3.5	−36.6	−2.8	6.3	2.3	−180	−40	1.8	1.8 ± 99	0.39E+04	3.8	0.59	56 ± 100	27 ± 99	0.43 ± 0.56	4.3 ± 11
112	GW 346.5−7.0	4.5	4.5	−12.6	16.7	...	...	...	...	8.5	1.3 ± 1.1	...	9.5	0.64	4.4 ± 4.1	1.5 ± 1.1	0.32 ± 1.02	3.8 ± 6.8
113	GW 350.7−3.5	5.0	6.0	−34.8	−0.5	5.7	2.9	−350	−50	8.5	4.2 ± 83	0.73E+05	9.3	0.56	61 ± 140	23 ± 83	0.39 ± 0.22	4.3 ± 34
114	GW 353.5+2.0	1.0	2.0	−2.0	2.0	...	...	...	...	1.8	1.9 ± 680	...	2.8	0.68	400 ± 650	410 ± 680	0.25 ± 0.36	48 ± 38
115	GW 353.7+9.7	2.5	1.0	−2.1	5.9	...	...	...	...	1.3	0.3 ± 1.3	...	1.5	0.73	1.9 ± 0.9	1.3 ± 1.3	1.13 ± 0.36	3.0 ± 71
116	GW 354.3−5.3	2.5	4.0	−29.8	7.4	5.6	2.9	−360	−150	4.5	0.9 ± 0.7	0.81E+04	2.0	0.42	5.5 ± 2.6	1.4 ± 0.7	0.21 ± 0.12	14 ± 12
117	GW 357.4+5.4	4.5	8.0	−12.2	−16.7	...	...	...	...	13.0	1.2 ± 11	...	7.5	0.56	5.0 ± 3.5	6.0 ± 11	0.28 ± 0.45	5.1 ± 12
118	GW 358.0−5.3	5.0	9.0	−20.3	24.4	...	...	...	...	12.0	1.9 ± 34	...	16.0	0.58	30 ± 95	7.3 ± 34	0.33 ± 0.39	7.5 ± 44

CATALOG OF WORM CANDIDATES

										H I PROPERTIES			INFRARED PROPERTIES					
NUMBER (1)	Name (2)	Δl (deg) (3)	Δb (deg) (4)	$v_{\min}$ (km s^{-1}) (5)	$v_{\max}$ (km s^{-1}) (6)	R_G (kpc) (7)	d (kpc) (8)	$z_{\min}$ (pc) (9)	$z_{\max}$ (pc) (10)	Area (deg^2) (11)	$\bar{N}_{\rm H\,I}$ (cm^{-2}) (12)	$M_{\rm H\,I}$ ($M_\odot$) (13)	Area (deg^2) (14)	r (15)	$\bar{I}_{100}$ (MJy sr^{-1}) (16)	$\bar{I}_{60}$ (MJy sr^{-1}) (17)	I_{60}/I_{100} (18)	$I_{100}/N_{\rm H\,I}$ (MJy sr^{-1}/10^{20} cm^{-2}) (19)
1	GW 0.5−5.9	1°5	7°5	−5.0	22.7	1.5	7.0	−1110	−180	8.3	2.2 ± 2.3	0.21E+06	6.8	0.74	10 ± 11	2.6 ± 2.3	0.29 ± 0.38	3.3 ± 4.2
2	GW 1.9+6.0	4.0	8.0	−10.8	26.1	4.1	4.4	110	730	15.0	0.9 ± 2.0	0.64E+05	10.0	0.67	8.7 ± 9.0	2.7 ± 2.0	0.28 ± 0.54	6.2 ± 50
3	GW 4.6−3.1	1.0	2.5	−0.8	26.1	5.0	3.6	−280	−120	3.3	1.5 ± 1.6	0.15E+05	2.3	0.74	15 ± 13	2.6 ± 1.6	0.20 ± 0.56	5.2 ± 5.0
4	GW 5.1−8.1	1.5	2.0	−3.9	24.6	5.6	3.0	−470	−360	3.3	0.9 ± 0.4	0.63E+04	1.5	0.57	3.0 ± 2.0	0.8 ± 0.4	0.21 ± 0.14	2.9 ± 14
5	GW 6.5−3.7	2.0	5.5	15.8	28.6	4.5	4.1	−460	−70	1.5	1.0 ± 1.8	0.62E+04	9.0	0.41	88 ± 190	1.7 ± 1.8	0.17 ± 0.20	4.6 ± 18
6	GW 9.4+8.0	2.0	2.0	17.9	22.2	5.5	3.1	380	490	1.5	1.2 ± 0.3	0.42E+04	1.8	0.46	1.5 ± 0.8	0.4 ± 0.3	0.26 ± 0.10	1.4 ± 3.1
7	GW 11.2+5.3	2.0	2.5	9.8	13.9	6.7	1.9	130	220	3.5	1.1 ± 0.9	0.34E+04	3.3	0.82	4.9 ± 3.6	1.4 ± 0.9	0.30 ± 0.29	6.3 ± 11
8	GW 12.3+1.8	2.5	2.0	21.2?	28.3?	5.6?	3.0?	50?	160?	3.0	2.7 ± 5.9	0.19E+05	1.8	0.65	27 ± 18	6.7 ± 5.9	0.34 ± 0.18	4.7 ± 10
9	GW 14.9−1.6	1.5	1.5	22.6	38.9	5.5	3.2	−140	−60	2.3	4 ± 370	0.22E+05	2.0	0.47	270 ± 470	230 ± 370	0.48 ± 0.26	19 ± 9
10	GW 16.4+6.4	4.0	6.5	−1.1	19.4	7.4	1.1	50	180	9.8	1.2 ± 0.3	0.39E+04	2.0	0.34	3.4 ± 1.9	0.7 ± 0.3	0.09 ± 0.16	3.8 ± 2.3
11	GW 16.9−3.8	1.5	3.5	19.5	30.7	6.1	2.5	−250	−90	1.8	3.8 ± 12	0.10E+05	4.0	0.66	26 ± 25	7.9 ± 12	0.34 ± 0.58	8.6 ± 3.2
12	GW 17.8+3.0	4.5	4.5	17.7	38.8	6.0	2.7	50	260	8.0	2 ± 160	0.31E+05	6.5	0.52	150 ± 230	87 ± 160	0.49 ± 0.34	17 ± 57
13	GW 19.5−6.4	3.5	7.5	19.6	45.2	5.9	2.8	−480	−100	9.3	0.9 ± 1.1	0.15E+05	12.0	0.56	7.1 ± 7.3	2.0 ± 1.1	0.32 ± 0.57	5.2 ± 4.6
14	GW 22.5−5.4	2.0	3.0	9.9	15.4	7.4	1.2	−150	−90	3.8	0.9 ± 0.6	0.12E+04	3.3	0.72	5.4 ± 2.8	2.0 ± 0.6	0.35 ± 0.08	8.0 ± 10
15	GW 23.0−1.6	2.0	1.5	48.2	108.4	4.4	4.9	−210	−80	3.0	6.5 ± 6.4	0.11E+06	1.5	0.71	12 ± 7	12 ± 6.4	0.62 ± 0.22	1.1 ± 7.2
16	GW 23.6+1.7	1.0	1.5	33.9	37.9	6.0	2.8	50	120	1.8	2.6 ± 6.9	0.88E+04	1.8	0.57	38 ± 35	12 ± 6.9	0.27 ± 0.15	13 ± 8
17	GW 24.7−7.1	5.0	6.5	−9.0	57.5	6.7	2.0	−350	−120	8.5	0.8 ± 0.4	0.71E+04	4.8	0.67	2.7 ± 1.5	0.5 ± 0.4	0.22 ± 0.50	3.1 ± 4.7
18	GW 28.5+3.9	2.0	3.0	28.8?	65.2?	5.9?	3.2?	140?	310?	5.0	30 ± 100	0.37E+06	2.0	0.55	190 ± 230	95 ± 100	0.42 ± 0.25	31 ± 108
19	GW 31.3+6.6	4.0	5.5	−7.7	26.0	7.9	0.7	50	120	6.3	1.4 ± 2.9	0.12E+04	8.8	0.54	5.7 ± 8.3	1.7 ± 2.9	0.24 ± 0.45	2.3 ± 49
20	GW 31.6−5.9	7.0	9.0	51.1?	104.7?	5.1?	4.8?	−850?	−80?	21.0	2.3 ± 13	0.28E+06	25.0	0.69	14 ± 34	6.0 ± 13	0.31 ± 0.64	3.5 ± 16
21	GW 35.3+6.5	2.5	5.0	7.6	22.8	7.6	1.1	80	180	7.3	1.9 ± 0.4	0.43E+04	6.3	0.78	3.5 ± 2.3	0.7 ± 0.4	0.18 ± 0.20	1.8 ± 3.2
22	GW 35.8−2.2	2.5	3.0	27.4	61.2	6.3	3.0	−210	−50	3.5	3 ± 40	0.24E+05	5.0	0.54	45 ± 64	28 ± 40	0.31 ± 0.17	3.0 ± 22
23	GW 38.9−9.2	3.0	2.0	13.1	29.5	7.4	1.5	−270	−220	3.5	1.0 ± 0.3	0.21E+04	3.8	0.76	1.6 ± 1.1	0.6 ± 0.3	0.31 ± 0.55	1.8 ± 29
24	GW 39.7+5.7	4.0	6.5	22.7	37.0	7.0	2.1	90	330	11.0	1.8 ± 0.5	0.20E+05	6.8	0.73	6.2 ± 5.2	1.5 ± 0.5	0.16 ± 0.07	2.3 ± 9.6
25	GW 40.0−5.5	7.5	6.0	14.3	51.7	6.9	2.3	−350	−100	8.8	2.0 ± 0.9	0.23E+05	7.3	0.60	2.9 ± 2.3	0.7 ± 0.9	0.17 ± 1.29	2.4 ± 2.7
26	GW 44.8−1.8	1.5	2.0	43.1	65.7	6.3	4.1	−220	−70	3.3	4.1 ± 2.1	0.54E+05	1.8	0.73	18 ± 15	4.3 ± 2.1	0.24 ± 0.20	7.1 ± 14
27	GW 46.4+5.5	7.0	6.0	25.3	38.2	7.1	2.3	80	330	17.0	1.7 ± 0.8	0.38E+05	7.3	0.59	3.4 ± 2.3	1.0 ± 0.8	0.27 ± 0.23	1.7 ± 1.7
28	GW 46.9−5.9	3.5	6.5	1.7	55.4	7.2	2.1	−350	−110	8.5	2.0 ± 0.4	0.18E+05	8.3	0.63	2.7 ± 1.8	0.6 ± 0.4	0.23 ± 0.12	1.5 ± 1.2
29	GW 47.9−1.8	2.5	2.5	56.8	76.7	...	...	...	...	2.3	5.8 ± 4.1	...	2.8	0.60	12 ± 11	11 ± 4	0.51 ± 1.49	3.4 ± 4.8
30	GW 49.7−8.6	3.0	3.0	26.0	30.0	7.3	2.2	−380	−270	4.8	1.2 ± 0.4	0.64E+04	4.8	0.84	2.8 ± 1.8	0.6 ± 0.4	0.19 ± 0.13	2.3 ± 2.7
31	GW 50.5+9.2	1.0	1.5	−8.6?	23.7?	8.1?	0.6?	90?	100?	2.0	0.6 ± 0.1	0.10E+03	2.0	0.63	1.5 ± 0.9	0.3 ± 0.1	0.18 ± 0.03	3.6 ± 11
32	GW 52.8−7.6	3.0	2.0	10.0	12.0	7.9	1.1	−170	−130	3.0	0.9 ± 0.2	0.88E+03	3.8	0.60	0.9 ± 0.8	0.3 ± 0.2	0.31 ± 1.25	0.6 ± 6.0
33	GW 54.5+7.5	5.0	5.0	18.2	49.8	7.1	3.2	250	520	8.0	1.8 ± 0.6	0.34E+05	11.0	0.69	2.1 ± 2.1	0.6 ± 0.6	0.25 ± 0.25	1.4 ± 1.0
34	GW 57.3−6.8	4.5	6.5	17.2	33.2	7.5	2.4	−400	−130	14.0	1.4 ± 0.3	0.27E+05	13.0	0.81	2.0 ± 1.6	0.6 ± 0.3	0.22 ± 0.40	1.4 ± 1.2
35	GW 60.0−3.4	1.5	1.5	24.5?	32.9?	7.4?	3.6?	−250?	−160?	2.0	1.5 ± 0.3	0.98E+04	1.3	0.63	3.6 ± 2.4	0.6 ± 0.3	0.16 ± 0.32	1.1 ± 3.5
36	GW 60.7+8.8	1.5	3.0	14.6	20.8	7.8	1.8	220	320	2.5	0.7 ± 0.1	0.14E+04	2.5	0.50	1.0 ± 0.6	0.3 ± 0.1	0.26 ± 0.48	1.0 ± 1.4
37	GW 60.9+2.6	4.0	5.0	−4.9	25.0	8.1	1.0	20	100	10.0	3.6 ± 1.6	0.81E+04	3.3	0.53	6.9 ± 7.6	3.1 ± 1.6	0.26 ± 0.21	1.4 ± 0.8
38	GW 63.1−6.5	5.0	6.5	5.0	15.5	8.0	1.4	−210	−60	3.3	1.5 ± 0.4	0.22E+04	13.0	0.42	2.8 ± 2.5	0.4 ± 0.4	0.21 ± 0.23	1.6 ± 5.0
39	GW 68.4−2.2	5.0	3.0	10.5?	18.3?	7.9?	2.3?	−160?	−40?	3.5	2.3 ± 8.7	0.11E+05	10.0	0.59	15 ± 15	5.2 ± 8.7	0.21 ± 0.19	2.7 ± 16
40	GW 73.3+7.8	6.5	4.0	−11.4	14.1	8.4	0.2	20	30	11.0	1.5 ± 1.3	0.13E+03	7.3	0.54	5.8 ± 5.9	1.9 ± 1.3	0.32 ± 0.19	3.4 ± 13
41	GW 78.1−4.7	5.5	9.0	1.6	8.7	...	...	...	...	2.8	1.1 ± 57	...	7.3	0.50	3.2 ± 2.6	12 ± 57	0.33 ± 1.52	3.0 ± 7.3
42	GW 89.7−2.4	2.5	3.0	−40.9?	−16.1?	9.8?	4.8?	−340?	−80?	4.5	3.0 ± 0.4	0.77E+05	2.5	0.52	7.3 ± 5.4	1.5 ± 0.4	0.13 ± 0.07	1.4 ± 16
43	GW 90.3+7.6	1.5	2.0	−2.1	1.9	8.5	0.2	20	30	1.5	1.3 ± 0.4	0.23E+02	2.0	0.72	3.2 ± 2.0	0.5 ± 0.4	0.15 ± 0.14	4.0 ± 2.8
44	GW 93.7+3.0	10.5	6.0	−21.4?	3.3?	8.9?	2.0?	40?	250?	32.0	5.8 ± 13	0.18E+06	23.0	0.64	21 ± 29	8.4 ± 13	0.30 ± 0.25	2.5 ± 9.0
45	GW 93.8+7.6	3.0	3.5	−2.1	2.9	...	...	...	...	2.5	1.2 ± 0.4	...	5.0	0.57	2.5 ± 1.4	0.4 ± 0.4	0.19 ± 0.24	0.8 ± 2.2
46	GW 99.4−1.7	2.0	1.5	−12.1	−7.3	8.9	1.6	−70	−30	2.5	3.4 ± 0.6	0.52E+04	2.3	0.53	3.0 ± 2.8	0.6 ± 0.6	0.22 ± 0.14	0.8 ± 2.5
47	GW 103.6−3.9	4.5	6.5	−66.0?	−14.0?	10.5?	4.4?	−580?	−80?	13.0	1.8 ± 3.7	0.11E+06	12.0	0.70	4.1 ± 8.3	1.8 ± 3.7	0.27 ± 0.55	0.9 ± 4.1
48	GW 104.2−9.0	1.0	2.5	1.4?	5.4?	...	...	...	...	2.5	0.7 ± 0.0	...	2.3	0.74	0.5 ± 0.4	0.2 ± 0.0	0.40 ± 0.73	0.6 ± 1.0
49	GW 107.4−3.3	3.5	5.0	−59.2	−50.7	11.5	5.6	−580	−100	7.8	1.9 ± 1.3	0.11E+06	5.0	0.68	3.0 ± 3.9	1.1 ± 1.3	0.29 ± 0.52	1.3 ± 3.1
50	GW 108.9−8.2	4.0	4.5	−31.1	−29.0	9.9	3.1	−540	−300	2.5	1.0 ± 0.2	0.58E+0.4	6.5	0.56	1.1 ± 0.8	0.3 ± 0.2	0.21 ± 0.22	0.8 ± 12
51	GW 112.7−4.0	11.0	8.5	−50.5	−34.2	10.7	4.1	−680	−70	15.0	2.3 ± 14	0.13E+06	26.0	0.58	12 ± 23	4.1 ± 14	0.26 ± 0.40	1.3 ± 2.2
52	GW 118.6−5.1	6.0	9.0	−49.0	−8.2	10.0	2.5	−450	−40	9.8	2.7 ± 2.5	0.41E+05	17.0	0.59	4.6 ± 5.4	1.2 ± 2.5	0.26 ± 0.36	1.7 ± 5.1
53	GW 123.4−1.5	4.0	1.5	−58.3?	−10.8?	10.5?	3.0?	−130?	−50?	2.0	2.3 ± 3.8	0.10E+05	3.5	0.66	5.9 ± 4.3	2.0 ± 3.8	0.36 ± 2.15	3.3 ± 6.5
54	GW 128.9−4.8	2.0	3.0	−61.2	−50.3	12.6	5.4	−570	−280	4.8	1.6 ± 0.3	0.53E+05	2.8	0.55	2.2 ± 1.6	0.5 ± 0.3	0.22 ± 0.27	0.9 ± 0.6
55	GW 129.8+1.6	1.5	1.5	−54.5	−26.2	11.2	3.6	60	160	3.0	2.6 ± 0.6	0.24E+05	2.0	0.61	4.1 ± 3.0	1.4 ± 0.6	0.28 ± 0.14	1.7 ± 0.9
56	GW 131.3−2.2	4.5	3.0	−59.6	−16.9	11.1	3.4	−240	−60	6.3	2.9 ± 2.4	0.50E+0.5	7.0	0.64	8.1 ± 7.3	2.1 ± 2.4	0.33 ± 0.96	1.2 ± 2.3
57	GW 132.6−9.0	4.5	2.0	−31.3	−22.9	10.2	2.3	−410	−330	4.0	1.4±0.7	0.72E+04	5.3	0.71	1.6 ± 1.8	0.6 ± 0.7	0.31 ± 0.40	1.6 ± 8.0
58	GW 134.6−4.7	2.0	2.5	−3.5?	2.1?	8.5?	0.1?	−10?	0?	2.8	1.9 ± 0.2	0.37E+01	3.8	0.62	0.7 ± 0.4	0.2 ± 0.2	0.50 ± 0.35	0.4 ± 2.2
59	GW 135.5+8.2	9.5	3.5	−36.2	0.6	9.6	1.5	170	260	8.0	1.3 ± 0.5	0.56E+04	13.0	0.54	3.3 ± 2.5	0.6 ± 0.5	0.16 ± 0.16	2.4 ± 3.4
60	GW 144.4+5.4	9.5	9.0	−50.7	−20.7	11.8	3.8	70	670	26.0	2.2 ± 0.2	0.19E+06	24.0	0.64	5.4 ± 11	0.3 ± 0.2	0.15 ± 0.20	1.2 ± 9.8
61	GW 148.1−4.8	14.5	8.0	−33.9	−13.1	10.6	2.4	−390	−40	21.0	2.2 ± 0.7	0.67E+05	45.0	0.48	3.7 ± 7.8	0.8 ± 0.7	0.24 ± 0.41	1.0 ± 16
62	GW 162.6+4.9	5.0	7.5	−46.3	−25.9	18.8	10.6	180	1580	21.0	1.8 ± 0.1	0.98E+0.6	9.8	0.54	1.0 ± 0.6	0.3 ± 0.1	0.21 ± 0.14	0.6 ± 0.9
63	GW 167.3+6.2	2.5	3.0	−6.1	−2.1	9.3	0.8	60	110	4.8	0.6 ± 0.1	0.44E+03	2.5	0.51	0.6 ± 0.4	0.2 ± 0.1	0.20 ± 0.19	1.0 ± 0.8

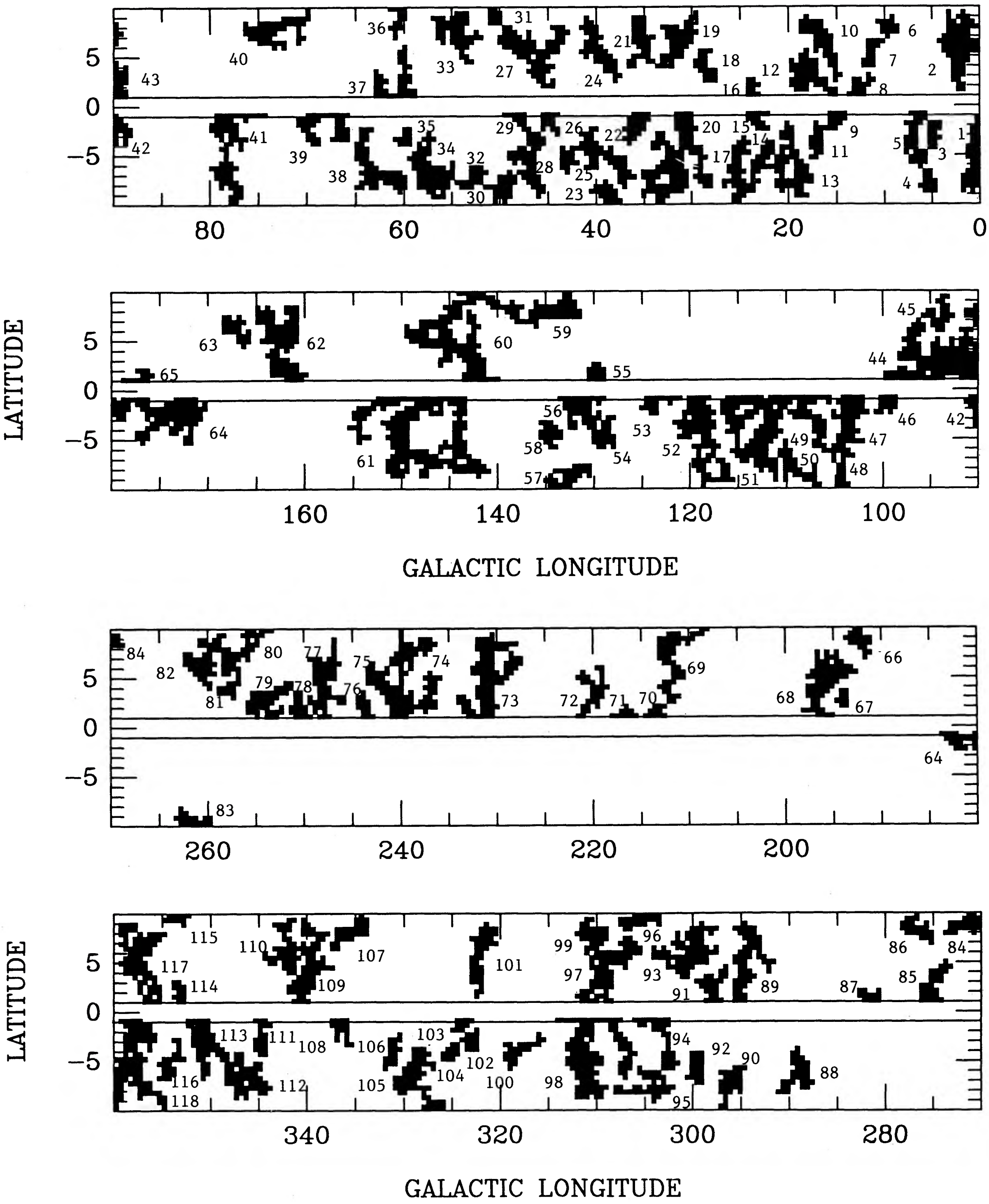

FIG. 2.—Finding chart of the 118 worm candidates. Each structure is labeled in an increasing order of l (Table 2).

Column (11) contains the area of the structure in H I. Columns (12) and (13) contain the average H I column density with rms deviation, and the H I mass, respectively. Column (14) contains the area of the structure at 100 μm. Column (15) contains the cross-correlation coefficient of the structure between H I and 100 μm. Columns (16) and (17) contain average 100 μm and 60 μm surface brightness with their rms deviations. Column (18) contains the median value of the 60 to 100 μm surface brightness ratio (obtained by the pixel-by-pixel comparison) with the rms deviation. Column (19) contains the median value of the 100 μm emissivity, i.e., $I_{100}/N_{\rm H\,I}$, with the rms deviation.

Table 3 lists radio continuum properties of the 35 structures that have counterparts at 408 MHz. Column (1) contains the name. Column (2) contains the area at 408 MHz. Column (3) contains the average 408 MHz brightness temperature with the rms deviation. Column (4) contains the cross-correlation coeffi-

1992ApJ...390..108K

TABLE 3

WORM CANDIDATES WITH ASSOCIATED RADIO CONTINUUM EMISSION

Name (1)	Area (deg^2) (2)	$\bar{T}_b$ (K) (3)	r (4)	$T_b/N_{\rm HI}$ (K/10^{20} cm^{-2}) (5)	r (6)	T_b/I_{100} (K/MJy sr^{-1}) (7)	r (8)	T_b/I_{60} (K/MJy sr^{-1}) (9)
GW 0.5−5.9	6.8	2.2 ± 1.6	0.80	1.1 ± 5.6	0.74	0.30 ± 0.33	0.79	0.9 ± 2.7
GW 6.5−3.7	3.5	4.5 ± 2.4	0.11	1.2 ± 0.0	0.62	0.34 ± 0.30	0.40	3.0 ± 3.5
GW 14.9−1.6	1.3	65.0 ± 56.0	0.30	4.8 ± 3.3	0.63	0.24 ± 0.25	0.68	0.4 ± 0.2
GW 16.4+6.4	4.0	1.8 ± 0.9	0.52	1.4 ± 4.2	0.53	0.66 ± 0.62	0.71	1.8 ± 8.6
GW 16.9−3.8	1.5	3.4 ± 2.9	0.46	0.2 ± 0.2	0.61	0.03 ± 0.03	0.58	0.1 ± 0.3
GW 24.7−7.1	3.5	2.6 ± 1.8	0.46	1.7 ± 6.9	0.61	1.00 ± 0.85	0.52	9.5 ± 17.8
GW 31.3+6.6	6.5	2.9 ± 2.1	0.75	2.3 ± 3.8	0.66	0.72 ± 0.66	0.83	3.4 ± 3.0
GW 31.6−5.9	8.8	5.8 ± 5.9	0.46	1.4 ± 2.1	0.54	0.27 ± 0.25	0.67	1.3 ± 2.0
GW 35.8−2.2	1.5	29.0 ± 30.0	0.11	0.9 ± 0.0	0.55	0.30 ± 0.26	0.34	0.1 ± 0.6
GW 44.8−1.8	1.3	1.5 ± 0.8	0.62	0.4 ± 0.7	0.85	0.05 ± 0.05	0.60	0.2 ± 0.9
GW 46.4+5.5	12.0	3.8 ± 2.1	0.71	2.1 ± 2.6	0.73	1.27 ± 1.10	0.82	4.6 ± 9.9
GW 68.4−2.2	3.8	1.6 ± 3.3	0.28	0.6 ± 3.4	0.61	0.11 ± 0.10	0.61	0.6 ± 1.0
GW 78.1−4.7	6.5	8.7 ± 9.5	0.00	...	0.00	...	0.61	0.5 ± 1.1
GW 89.7−2.4	2.0	1.4 ± 0.5	0.67	0.2 ± 1.4	0.67	0.12 ± 0.10	0.67	0.9 ± 0.6
GW 93.8+7.6	2.3	1.5 ± 1.4	0.21	0.5 ± 0.4	0.45	0.55 ± 0.51	0.63	2.9 ± 3.3
GW 103.6−3.9	8.5	2.0 ± 3.1	0.60	0.5 ± 2.1	0.73	0.56 ± 0.49	0.83	2.0 ± 4.3
GW 123.4−1.5	3.0	1.6 ± 0.8	0.82	0.9 ± 1.1	0.69	0.37 ± 0.33	0.77	0.7 ± 2.3
GW 131.3−2.2	4.5	1.0 ± 0.5	0.66	0.4 ± 0.5	0.53	0.09 ± 0.09	0.60	0.5 ± 1.3
GW 132.6−9.0	2.8	1.3 ± 1.2	0.75	1.8 ± 12.5	0.59	0.56 ± 0.50	0.59	1.1 ± 5.1
GW 167.3+6.2	1.0	0.6 ± 0.5	0.34	0.9 ± 0.5	0.47	0.50 ± 0.55	0.63	1.0 ± 7.6
GW 175.8−2.5	12.0	3.2 ± 3.5	0.71	1.2 ± 6.3	0.56	0.34 ± 0.32	0.75	0.9 ± 7.4
GW 253.9+2.6	6.3	1.4 ± 1.0	0.40	0.2 ± 0.6	0.64	0.63 ± 0.53	0.80	4.7 ± 10.5
GW 260.9+6.1	5.0	2.0 ± 1.2	0.51	1.3 ± 3.4	0.83	1.61 ± 1.42	0.86	3.8 ± 6.6
GW 274.7+2.7	1.8	0.8 ± 0.4	0.50	0.5 ± 0.3	0.57	0.68 ± 0.69	0.71	1.9 ± 2.7
GW 289.0−6.6	3.5	1.4 ± 1.4	0.61	0.7 ± 0.9	0.66	0.35 ± 0.33	0.67	0.8 ± 2.8
GW 294.2+5.1	8.3	2.0 ± 1.0	0.75	1.6 ± 1.3	0.63	0.61 ± 0.62	0.48	1.2 ± 1.3
GW 310.3−4.7	12.0	4.5 ± 4.5	0.53	1.1 ± 2.5	0.67	0.50 ± 0.45	0.70	1.5 ± 2.0
GW 310.4+7.8	1.3	0.4 ± 0.3	0.44	0.2 ± 0.2	0.51	0.09 ± 0.09	0.51	0.6 ± 0.4
GW 328.7−7.0	1.8	1.0 ± 0.9	0.12	0.1 ± 0.2	0.39	0.39 ± 0.36	0.41	1.0 ± 1.3
GW 336.5−2.0	2.5	19.0 ± 12.0	0.65	10.0 ± 10.5	0.73	0.10 ± 0.09	0.73	0.4 ± 0.2
GW 340.0+4.8	6.3	2.3 ± 1.5	0.52	0.9 ± 1.5	0.74	0.16 ± 0.15	0.58	0.6 ± 0.8
GW 342.5+6.4	5.8	2.2 ± 1.5	0.46	0.9 ± 2.5	0.67	0.38 ± 0.34	0.74	1.4 ± 6.8
GW 346.5−7.0	7.5	3.0 ± 1.9	0.56	1.6 ± 7.5	0.74	0.56 ± 0.54	0.72	2.1 ± 7.1
GW 353.5+2.0	1.3	100.0 ± 100.0	0.51	9.8 ± 4.7	0.67	0.15 ± 0.15	0.79	0.3 ± 0.2
GW 358.0−5.3	7.3	4.0 ± 600.0	0.32	4.0 ± 22.2	0.51	0.63 ± 0.54	0.55	2.3 ± 13.1

cient of the structure between 408 MHz and H I. Column (5) contains the median values of the ratio of the 408 MHz brightness temperature to the H I column density, and its rms deviation. Column (6) contains the cross-correlation coefficient of the structure between 408 MHz and 100 μm. Column (7) contains the median value of the 408 MHz brightness temperature to the 100 μm surface brightness ratio with rms deviation. Column (8) contains the cross-correlation coefficient of the structure between 408 MHz and 60 μm. Column (9) contains the median value of the 408 MHz brightness temperature to the 60 μm surface brightness ratio with rms deviation.

4. STATISTICS FOR WORM CANDIDATES

4.1. *Basic Statistics*

We first look at the selection effect due to our spatial filtering, which affects the statistics that will be discussed below. Figure 3 shows the distribution of the worm candidates in the (D, d) plane, where D is the characteristic linear size (square root of the area in H I) and d is the distance. In Figure 3, structures below the solid line, which is a stringent lower limit set by our requirement that a structure must occupy more than or equal to 5 pixels, cannot be detected. The structures above the dotted line, which is an upper limit set by our filter size, are generally difficult to detect unless they are thin and long. Most structures fall between these two limits. Hence, an obvious selection effect of our technique is to detect only small structures at a closer distance, and vice versa. For structures between the two limits, the detectability with our technique depends not on their angular sizes but also on their brightness relative to the forground and background gas, which depends on their locations in the Galaxy. This incompleteness should be kept in mind in the following discussion of basic statistics.

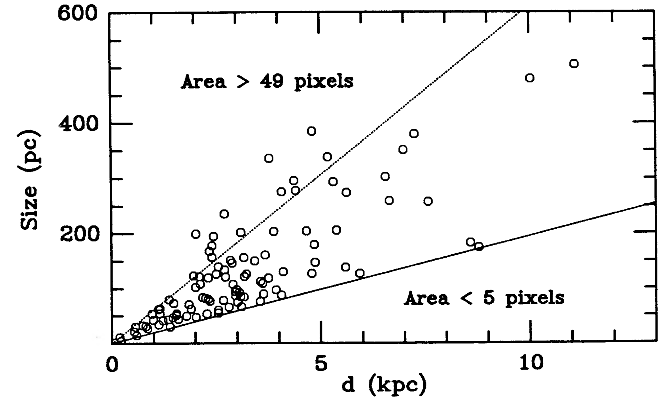

FIG. 3.—Plot of the sizes of the worm candidates vs. their distances. The solid line is a stringent lower limit set by our requirement that a structure must occupy more than or equal to 5 pixels. The dotted line is an upper limit set by our filter size.

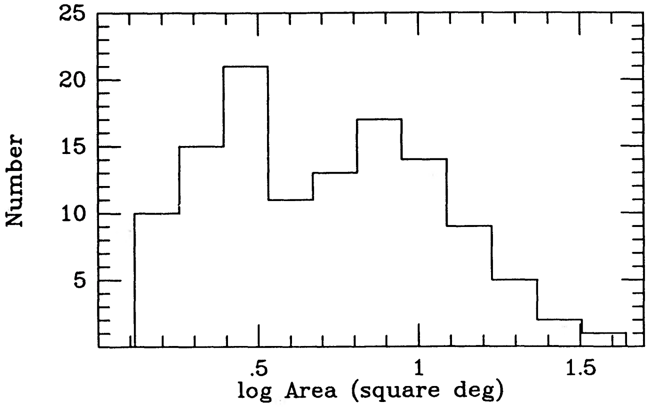

FIG. 4.—The distribution of areas occupied by each structure in H I

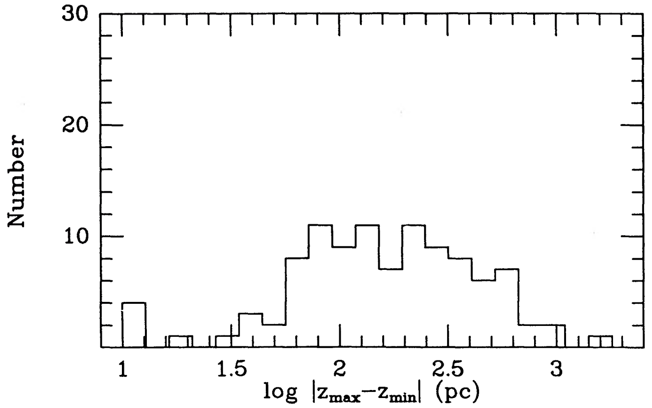

FIG. 6.—The distribution of the linear length, $|z_{\max} - z_{\min}|$, of each structure

Figure 4 shows the distribution of areas occupied by the worm candidates in H I, where we can see that the number of worm candidates per unit logarithmic interval is roughly constant for areas smaller than ~10 square degree and decreases for larger areas due to our filter size, i.e., 3°.5 × 3°.5. The cutoff at 1.25 square degrees occurs because we neglected structures smaller than 5 pixels. The median value is 4.8 square degree. The distribution of areas at other frequencies is basically similar.

Figure 5 shows the distribution of distances to the worm candidates. It has a relatively strong peak between 2 and 3.5 kpc. The median value is 2.8 kpc. One expects the surface density of "interstellar structures" such as the ones detected in this paper to be either roughly constant in the inner Galaxy or, if they are associated with superbubbles, to peak in the "molecular ring" where the OB star formation rate is high, and then to decrease drastically in the interior "hole" of the Galaxy where there is not much interstellar gas. Therefore, the number of structures between d and $d + \Delta d$ should rise with d until $d \approx 5$ kpc and should be more or less flat for larger d. The steep decrease at $d > 3$ kpc in Figure 5 then suggests that our detectability decreases sharply at $d > 3$ kpc, which is probably partly due to the decrease in intrinsic number of structures per unit size interval with increasing size.

Figure 6 shows the distribution of the linear length, $|z_{\max} - z_{\min}|$. The number of structures per unit logarithmic interval is roughly constant. The median value is 160 pc. Using the median values of the area and the distance, the characteristic width of the worm candidates is 70 pc.

Figure 7 shows the distribution of average H I column density of the worm candidates. The median value is 1.7×10^{20} cm^{-2}. (The structures that has an exceptionally large average H I column density, 3×10^{21} cm^{-2}, is GW 28.5+3.9, which is possibly associated with the W40 complex region.) If we assume that the line-of-sight extent is roughly same as the width which is 70 pc, then the characteristic volume density of the structures is 0.8 cm^{-3}. Figure 8 shows the distribution of H I mass, and it has a steep cutoff at $\sim 2 \times 10^5\ M_\odot$ and a tail toward the smaller masses. The steep cutoff at large mass is associated with the cutoff in the area due to our filter size. The median value of the H I mass is $1.0 \times 10^4\ M_\odot$.

Figure 9 shows shows the distribution of average 100 and 60 μm surface brightnesses. The median value of the average 100 and 60 μm surface brightness are 3.5 and 1.0 MJy sr^{-1}, respectively. Table 4 summarizes the characteristic values of various physical parameters of the worm candidates.

4.2. *Correlation with* H II *Regions*

We cross-correlated our catalog with the catalog of H II regions, because, if a superbubble is young, it is expected to have an associated H II region. For northern H II regions, we used the catalog of Blitz, Fich, & Stark (1982), which lists parameters of Sharpless (1959) H II regions plus an additional

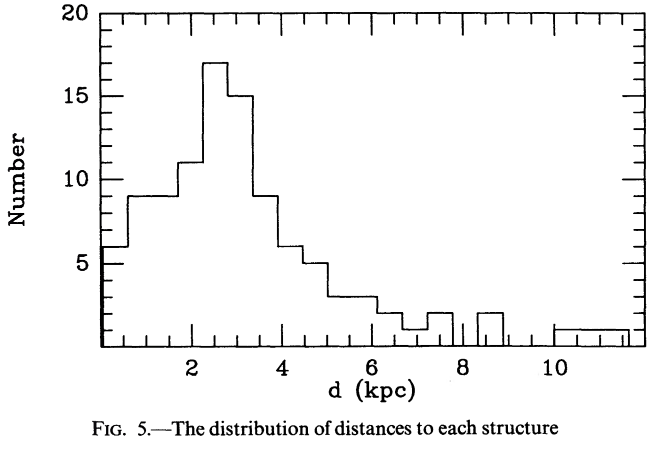

FIG. 5.—The distribution of distances to each structure

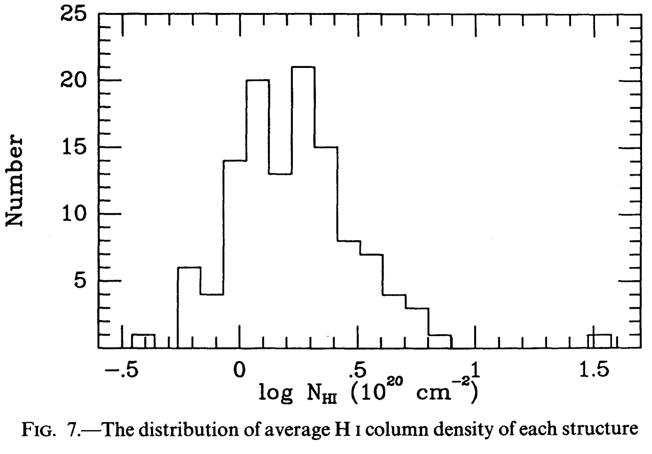

FIG. 7.—The distribution of average H I column density of each structure

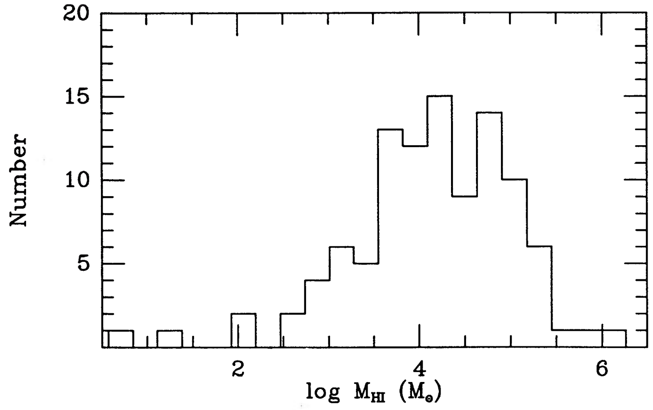

FIG. 8.—The distribution of H I mass of each structure

TABLE 4

CHARACTERISTIC PARAMETERS OF THE WORM CANDIDATES

Parameter	Characteristic Value	Unit
Angular area	4.8	square degree
Length	160	pc
Width	70	pc
$N_{\rm H\,I}$	1.7×10^{20}	cm^{-2}
$n_{\rm H\,I}$	0.8	cm^{-3}
$M_{\rm H\,I}$	1.0×10^{4}	$M_{\odot}$
I_{100}	3.5	MJy sr^{-1}
I_{60}	1.0	MJy sr^{-1}

65 smaller (BFS) H II regions. For southern ($260° < l \leq 350°$) H II regions, we used the catalog of Rogers, Campbell, & Whiteoak (1960). (There is also a comprehensive catalog of H II regions along the whole Galactic equator by Marálková 1974, which we found only after this work.) From the central positions and the angular radii of H II regions is these catalogs, we first determined the H II regions that geometrically overlap the worm candidates using Figure 2. We also determined the H II regions that do not overlap but are located in the plane ($|b| \leq 1\overset{\circ}{.}5$) right below the worm candidates. Then we determined whether the H II region velocities overlap the velocity of the worm candidates. (To be more specific, we determined whether the velocity range, $v_{\rm center} - \Delta v_{\rm FWHM}$ to $v_{\rm center} + \Delta v_{\rm FWHM}$, of an H II region overlaps the velocity range, $v_{\rm min}$ to $v_{\rm max}$, of a worm candidate.) For northern H II regions, we used the Hα velocity of Fich, Treffers, & Dahl (1990), who observed Hα lines toward 284 objects in the catalog of Blitz et al. Among 65 BFS H II regions, however, only 12 objects have been observed in the Hα line, and we used the CO velocity of Blitz et al. for the remaining BFS objects. For southern H II regions, we used the H109α recombination line velocity of Wilson et al. (1970).

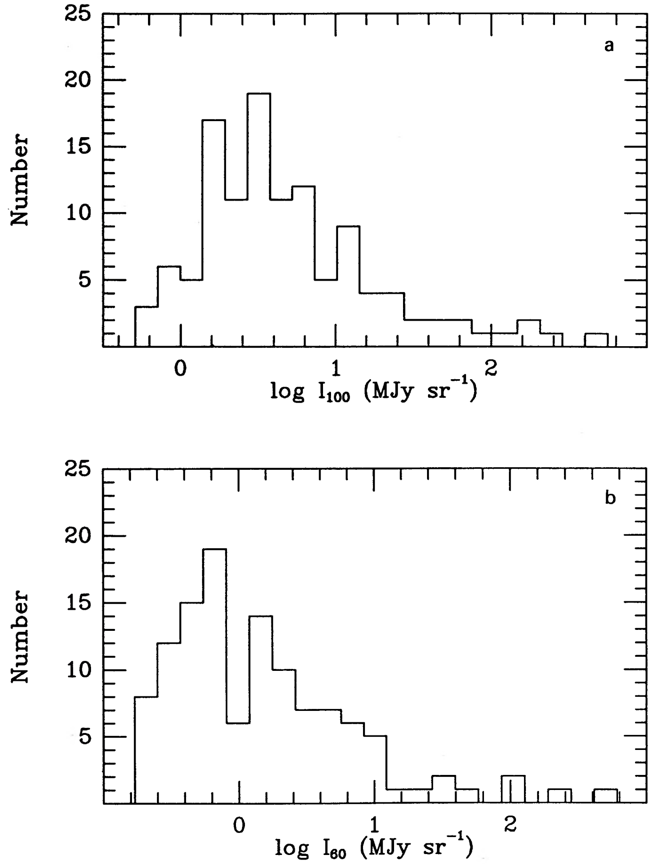

FIG. 9.—The distribution of (*a*) average 100 μm and (*b*) average 60 μm surface brightness of each structure.

In this way, we have found 52 worm candidates that possibly have associated H II regions: 37 with geometrically overlapping H II regions, and the remaining 15 with H II regions located right below them at the plane. They are listed in Table 5, where column (1) lists the name of worm candidates, column (2) lists the H II regions that geometrically overlap, and the third column lists the H II regions that do not overlap but are located right below the worm candidates at the plane. The H II regions whose velocity has not been measured by Fich et al. or by Wilson et al. are marked with a question mark. Among these 52 H II region–associated candidates, 24 have associated radio continuum emission and are listed in Table 3.

4.3. *Correlations among Physical Properties*

Figure 10 shows the correlation between the 100 μm intensity I_{100} and the H I column density $N_{\rm H\,I}$, where the triangles and the circles represent the structures with and without an associated H II region, respectively. The structures that have a large dispersion, i.e., with an rms dispersion larger than 3 times the average value, are marked by either open circles or open triangles. Figure 10 clearly shows that the structures brighter at 100 μm have a larger H I column density. Also, it shows that most points lie above the solid line, which represents the relationship in the solar neighborhood, i.e., $I_{100}/N_{\rm HI} \approx 1.0$ MJy sr^{-1}/10^{20} cm^{-2} (Beichman 1987; Heiles, Reach, & Koo 1988; Désert, Boulanger, & Puget 1990). We can think of at least three reasons for this apparent 100 μm excess: (1) the general increase of the 100 μm emissivity toward the Galactic interior due to the increase of the diffuse interstellar radiation field (ISRF), (2) associated H II regions, in which case $I_{100}/N_{\rm H\,I}$ increases because of dust heating by Lyα photons and because some of the gas is ionized, and (3) associated molecular gas. An increased $I_{100}/N_{\rm H\,I}$ occurs because of the presence of molecular gas in isolated clouds in the Solar neighborhood (Heiles et al. 1988). If molecular gas is positionally correlated with atomic gas, as it is likely to be for our linear resolution of these objects, then some of the infrared emission might well be associated with molecular gas. However, this effect is *not* expected to be very significant for most cataloged structures in the inner Galaxy, because we

TABLE 5

WORM CANDIDATES NEAR H II REGIONS

Worm Candidate (1)	H II Regions that Overlap (2)	H II Regions at the Plane (3)	Remarks (4)
GW 0.5−5.9	...	S17, S19, S20	
GW 6.5−3.7	S25, S29, S31, S32	S26, 28, S30, BFS1	
GW 12.3+1.8	S38, S42	S37, S39, S40? S41, S43, S44	a
GW 14.9−1.6	S45	S44, S47	
GW 16.4+6.4	S46	...	
GW 17.8+3.0	S49?, S54	S45, S47, S53	
GW 23.0−1.6	...	S56	
GW 23.6+1.7	...	S57, S58	
GW 28.5+3.9	S64	...	a
GW 31.3+6.6	S68	...	
GW 31.6−5.9	...	S66, S67, S69	a
GW 35.8−2.2	S72	...	
GW 46.4+5.5	S78	...	
GW 47.9−1.8	S79	...	
GW 60.9+2.6	S91	S86, S87?, S88, S89?, S90	
GW 68.4−2.2	S109?, BFS2	S97 to S100	a,b
GW 73.3 + 7.8	S109?	...	
GW 78.1−4.7	S107, S109?	S104?, S106, S108	
GW 89.7−2.4	S109?, S119	S121, BFS5	a,b
GW 93.7+3.0	S120, S121, S128, S131, BFS4, BFST	S124, BFS5, BFS6, BFS8	a,b
GW 103.6−3.9	S132	S134?, S135	a
GW 107.4−3.3	S147, S148, S151 to S153	S144?, S146, S149, BFS12	b
GW 112.7−4.0	S142, S143, S157, S164, S166, S168, S169	S138?, S139, S147, S148, S156, S158, S161 to S163, S165, BFS14 to BFS17, BFS19?	b
GW 118.6−5.1	S172, S173	...	
GW 123.4−1.5	S185, BFS21	S179?, S180	a,b
GW 131.3−2.2	...	S190	
GW 144.4+5.4	S202, S204	S203, BFS26?, BFS27	b
GW 148.1−4.8	S203, S205, S206, BFS31	S209, BFS34	c
GW 162.6+4.9	BFS44	...	b
GW 175.8−2.5	S229, S230, S236	S234, S237, S242, BFS48	b
GW 195.7+4.5	...	S266, S269	
GW 213.4+1.4	...	S284, S285	
GW 216.6+1.3	...	S286, S287, BFS55 to BFS59	
GW 230.8+5.2	S299?, S300	S302, S305	
GW 247.9+4.6	S312	...	a
GW 257.5+8.1	S312	...	
GW 274.7+2.7	...	RCW42?	
GW 281.5+1.5	...	RCW45?, RCW46	a
GW 294.2+5.1	RCW59?	RCW62	a
GW 303.2−3.1	...	RCW75?	
GW 308.8+4.2	...	RCW79, RCW80?, RCW82?, RCW83?	
GW 310.3−4.7	RCW83?	RCW78 to RCW80, RCW82?, RCW85?	a
GW 322.0+5.7	...	RCW92	a
GW 336.5−2.0	...	RCW107	
GW 340.0+4.8	RCW113?	RCW110, RCW111	a
GW 342.5+6.4	RCW113?	...	a
GW 344.9−2.8	RCW113?, RCW114?	...	
GW 346.5−7.0	RCW114?	...	
GW 350.7−3.5	...	S8, S11	
GW 353.5+2.0	S10, S11	...	
GW 357.4+5.4	S12, S13	...	
GW 358.0−5.3	S15	S12, S16?	

[a] Velocity of the worm candidate is uncertain.

[b] Velocity of BFSs is based on CO observations of Blitz et al.

[c] Velocity of BFS31 is based on CO observations of Blitz et al.

excluded the central ($-1° < b < +1°$) portion of the Galactic plane where most molecular gas resides. The effect of associated H II regions can be seen in Figure 10, where the triangles are generally located higher than the circles. The average 100 μm emissivity, $I_{100}/N_{\rm H\,I}$, of the structures with associated H II regions is 7.1 ± 2.2 MJy sr^{-1}/10^{20} cm^{-2}, which is considerably larger than 3.1 ± 0.9 MJy sr^{-1}/10^{20} of those structures without associated H II regions.

The increase of the 100 μm emissivity toward the Galactic interior can be seen in Figure 11, where the ratio $I_{100}/N_{\rm H\,I}$ (col. [19] in Table 2) of only those structures *without* an associated H II region is plotted as a function of the Galactocentric radius. In Figure 11, the open circles are again the ones which have an rms deviation larger than 3 times their median value, and the area inside the circle is proportional to the 100 μm intensity (normalized by 25 MJy sr^{-1}). Figure 11 clearly shows the trend

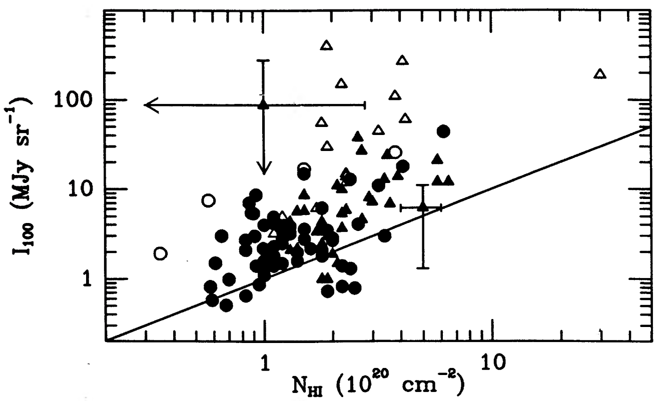

FIG. 10.—The average 100 μm surface brightness I_{100} vs. the average H I column density $N_{\rm H\,I}$ of each structure. The triangles and circles represent the structures with and without associated H II regions, respectively. For several structures, 1 σ deviations are shown. The structures with large error bars are marked by open symbols. The straight line represents the relationship at high galactic latitudes, i.e., $I_{100}/N_{\rm H\,I} = 1.0$ MJy sr^{-1}/10^{20} cm^{-2}.

such that the 100 μm emissivity increases toward the Galactic interior, although there is a large scatter. The average values at 2 kpc intervals (filled squares with error bars) are 7.6 ± 5.3, 3.7 ± 2.5, 2.5 ± 2.9, 1.1 ± 0.8, and 1.2 ± 1.0 at R = 4–6, 6–8, 8–10, 10–12, and 12–15 kpc, respectively. It is not completely ruled out that the increase of $I_{100}/N_{\rm H\,I}$ is partly due to the associated molecular gas, particularly for those structures in the "molecular ring." But, as we pointed out in the above, the contribution to the 100 μm intensity in Figure 11 from molecular gas is not likely to be very significant because each data point is obtained from a pixel-by-pixel comparison of the 100 μm map with the H I map excluding the central ($-1° < b < +1°$) portion of the Galactic plane. Also, Bloemen, Deul, & Thaddeus (1990), who decomposed the total 100 μm intensity radially by cross-correlating with H I and CO emission, found a similar trend for grains associated not only with H I but also with CO. Hence, we conclude that the increase of the infrared emissivity in Figure 11 is due to the increase of the general ISRF, which is consistent with the result of Mathis, Mezger, & Panagia (1983) that the diffuse ISRF increases by a factor of ~7 at $R = 4$ kpc.

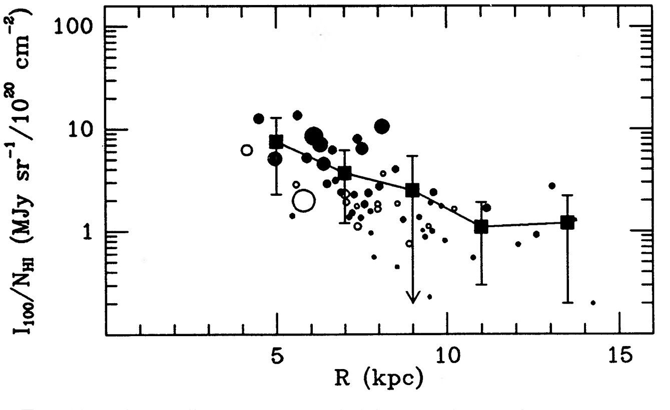

FIG. 11.—The median 100 μm emissivity, $I_{100}/N_{\rm H\,I}$, of each structure without an associated H II region as a function of Galactocentric radius. The open circles are again the ones which have a large rms deviation. The area under the circle is proportional to the 100 μm intensity (normalized by 25 MJy sr^{-1}). The filled squares with error bars represent the average values at 2 kpc interval.

The average I_{60}/I_{100} worm candidates (excluding ones with a large dispersion) is 0.28 ± 0.03 (corresponding to the grain temperature of 27 ± 1 K using the $\lambda^{-1.5}$ emissivity law), which is considerably larger than the 0.21 ± 0.02 in the solar neighborhood (Boulanger & Pérault 1988; Heiles et al. 1988; Désert et al. 1990). Bloemen et al. (1990) obtained a similar value, 0.27 ± 0.03. The 60–100 μm intensity ratio depends mainly on the grain size distribution. According to Draine & Anderson (1985), the ratio increases from 0.174 to 0.240 for the MRN size distribution (Mathis, Rumpl, & Nordsieck 1977; minimum grain radius of 3 Å) as the ISRF increases by a factor of 3 from its intensity in the solar neighborhood, whereas it increases from 0.234 to 0.287 for a grain size distribution with enhanced small-size grains. For comparison, in a recent empirical model by Désert et al. (1990), where very small grains (radius between 12 and 150 Å) and PAHs both constitute 7% of total grains in mass, the ratio increases from 0.20 to 0.24. Hence, the average ratio 0.28 ± 0.03 seems to require a considerable enhancement of small-size grains in the worm candidates.

We see neither a systematic variation of I_{60}/I_{100} with Galactocentric radius nor a difference between the structures without H II regions, 0.28 ± 0.04, and those with H II regions, 0.28 ± 0.06, (see Fig. 2 of Koo et al. 1990). Both would be expected if this ratio depends on the ISRF to a significant extent. Thus, we conclude that the higher value of I_{60}/I_{100} in the worm candidates is a result of the grain size distribution instead of the ISRF intensity. However, this conclusion is not absolutely certain because the data in Table 2 may have too large a dispersion to show the variation of the ratio with the intensity of the radiation field.

Figure 12 shows the average 408 MHz brightness temperature T_b versus the average 60 μm intensity of each structure. *For the structures with associated* H II *regions*, there is a good correlation between the two, which suggests that *the* 408 MHz *continuum is likely to be a thermal emission.* In Figure 12, the straight line is the expected relationship for a diffuse H II region by assuming that all the Lyα photons are used to heat the dust grains. The brightness temperature of the thermal free-free emission at 408 MHz from an optically thin source is (Osterbrock 1989)

$$T_b \simeq 0.54 T_e^{-0.35}\ {\rm EM}\ , \qquad (2)$$

where T_e is the gas kinetic temperature and EM (cm^{-6} pc) is

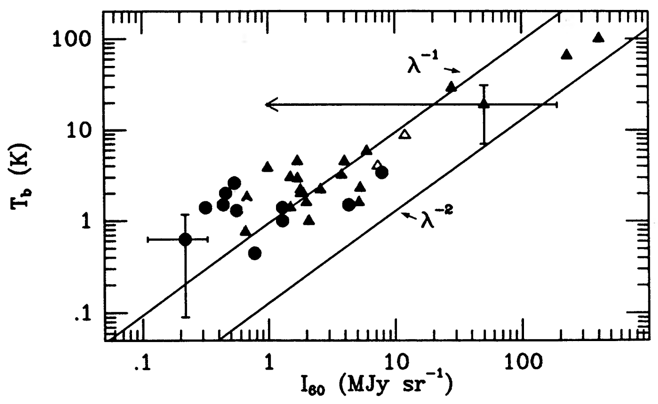

FIG. 12.—The average 408 MHz brightness temperature T_b vs. the average 60 μm intensity I_{60} for each structure (see Fig. 10 for the explanation of symbols). The straight lines are the expected relationships for a diffuse H II region for $\lambda^{-1.0}$ and $\lambda^{-2.0}$ emissivity law (see text).

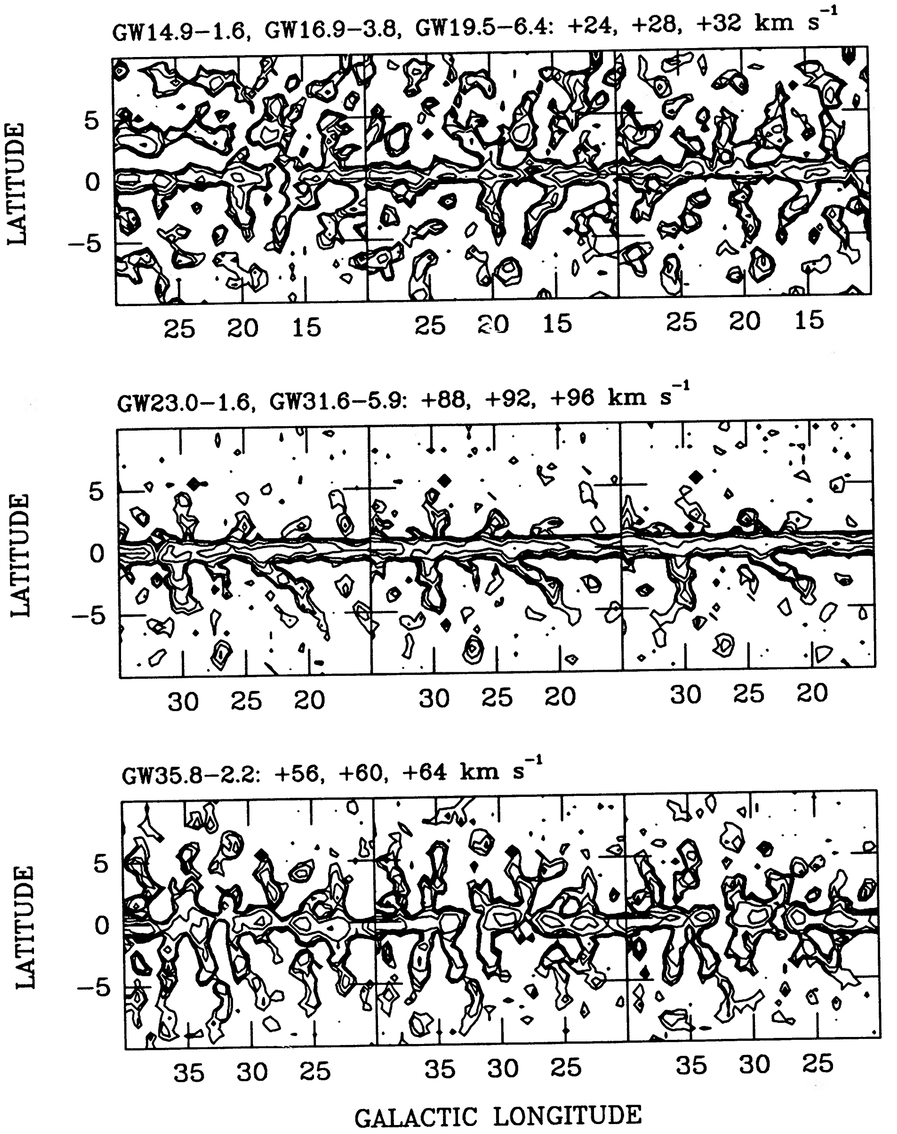

FIG. 13.—Channel maps of some individual objects (see § 5). For each object, three channel maps are shown. Each channel map is obtained by integrating over 4 km s^{-1}, and its central velocity, together with name(s) of the object, is shown above the picture. The contour intervals (in K km s^{-1}) are 2, 5, 10, 20, 50, 100, and 200.

the emission measure. If all the Lyα photons are absorbed by dust grains and re-emitted as infrared emission, then the total infrared surface brightness integrated over frequency is (Osterbrock 1989)

$$\int_0^\infty I_\nu\, d\nu \simeq \frac{h\nu_{\mathrm{Ly}\alpha}}{4\pi}(\alpha_B - \alpha_{2^2S}^{\mathrm{eff}})\ \mathrm{EM}$$
$$= 1.27 \times 10^{11}\ \mathrm{EM\ MJy\ Hz\ sr^{-1}}\ , \quad (3)$$

where $h\nu_{\mathrm{Ly}\alpha} = 10.2$ eV is the energy of the Lyα photon, α_B is the recombination coefficient excluding the ground level, and $\alpha_{2^2S}^{\mathrm{eff}}$, which has been subtracted to account for the two photon process, is the effective recombination coefficient for populating $2\,^2S$ by direct recombinations and by recombinations to higher levels followed by cascades to $2\,^2S$. At $T_e = 5000$ K, $\alpha_B = 4.54 \times 10^{-13}$ cm^3 s^{-1} and $\alpha_{2^2S}^{\mathrm{eff}} = 1.38 \times 10^{-13}$ cm^3 s^{-1}. The fraction of the infrared emission emitted at 60 μm depends rather sensitively on the infrared emissivity law. Using $T_d = 27$ K, we have $I_{60}/\int I_\nu\, d\nu = 2.3 \times 10^{-13}$ Hz^{-1} and 17×10^{-13} Hz^{-1} for $\lambda^{-1.0}$ and $\lambda^{-2.0}$ emissivity law, respectively. Therefore

$$\frac{T_b}{I_{60}} \simeq \begin{cases} 0.93 \text{ for } \lambda^{-1.0} \text{ emissivity law}\ , \\ 0.13 \text{ for } \lambda^{-2.0} \text{ emissivity law}\ , \end{cases} \quad (4)$$

where we used $T_e = 5000$ K. In Figure 12, equation (4) is represented by two straight lines, and seem to describe the trend. Faint sources, however, are generally brighter at 408 MHz than what we expect from equation (4). This may suggest that the 408 MHz emission in these faint structures is mostly nonthermal, as in the North Polar Spur (see Heiles et al. 1980). We are currently carrying out a radio recombination line observation in order to find out the nature of the continuum emission.

5. DESCRIPTION OF SOME INDIVIDUAL CANDIDATES

5.1. *GW 14.9 − 1.6, GW 16.9 − 3.8, and GW 19.5 − 6.4*

These three structures, in the Sagittarius arm, appear between $v_{\mathrm{LSR}} = +20$ and $+44$ km s^{-1}, and are most clearly

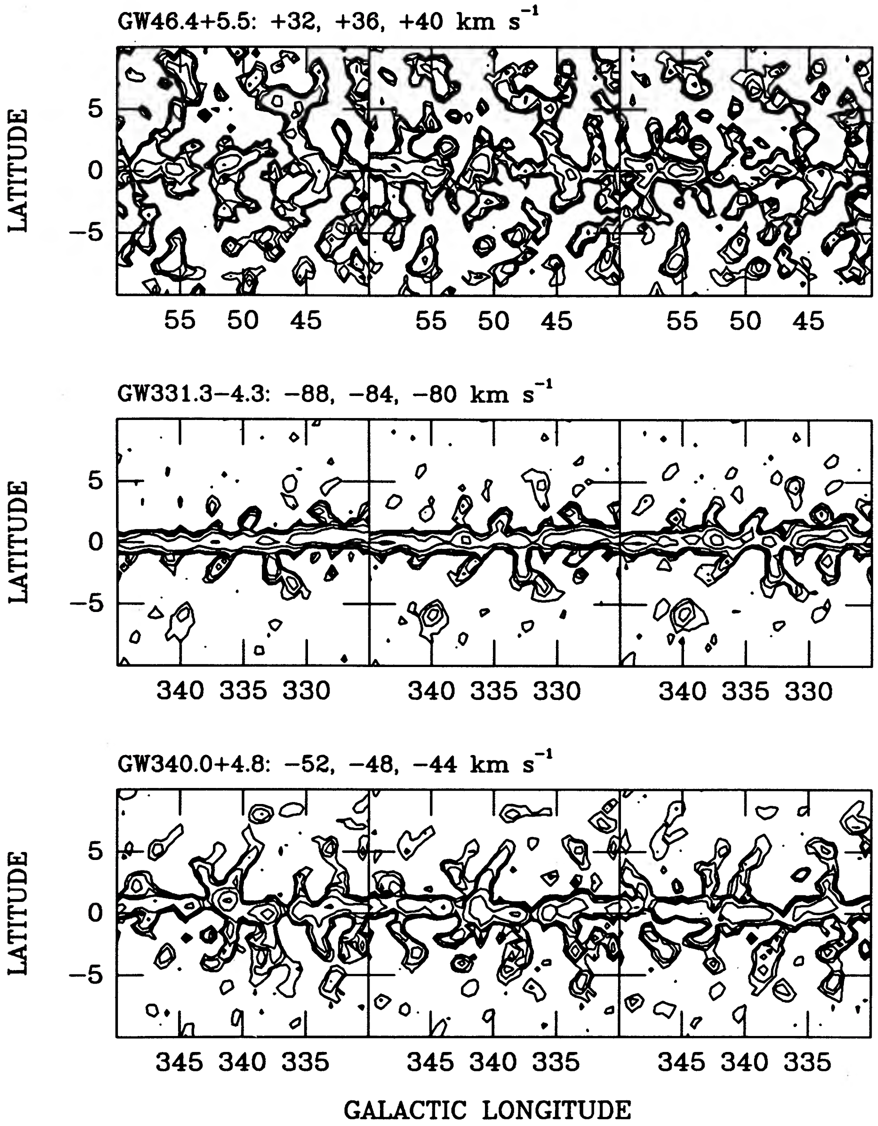

FIG. 13.—*Continued*

seen in channel maps centered at $v_{\rm LSR} = +24$, $+28$, and $+32$ km s^{-1} (Fig. 13). In Figure 13, we can see two prominent vertical structures in the lower plane ($b < 0°$); one at $l \simeq 16°$ and the other at $l \simeq 20°$. The latter has been cataloged as GW 19.5−6.4, whereas the former has been cataloged as two separate objects; GW 14.9−1.6 and GW 16.9−3.8. These two vertical structures, facing each other, are separated by $\sim 6°$, or 300 pc at $d \sim 3$ kpc. The lengths of the structures are comparable to their separation. The morphology and their sizes suggest that the two are possibly the walls surrounding a superbubble. A candidate for the energy source is Ser OB1 association, which currently has eight O stars including one O4 and two O5 stars between $l = 15°$ and 19° (Humphreys 1978).

There is 408 MHz continuum emission associated with both structures. (Fig. 13 is at the same scale as Figure 1, so that one can compare them directly.) The continuum emission associated with GW 14.9−1.6 is very strong, and is probably the thermal emission associated with the H II region M17 (S45). Although it has not been cataloged, GW 19.5−6.4 also seems to have associated 408 MHz emission.

5.2. *GW 23.0−1.6*

There seem to be two distinct objects along this line of sight: one between $v_{\rm LSR} = +80$ and $+120$ km s^{-1} and the other between $v_{\rm LSR} = +44$ and $+72$ km s^{-1}. We shall call the former GW 23.0−1.6+100, and the latter GW 23.0−1.6+60. GW 23.0−1.6+100 is very prominent, and is tilted to the plane by $\sim 40°$ (Fig. 13). In addition to the H II region S56 listed in Table 5, which is small $\sim 7'$ and at somewhat different velocities (l, b, $v_{\rm LSR}$) = (22°.0, +0°.0, +69 km s^{-1}), there are two giant *radio* H II regions in this region ($20° < l < 24°$): G22.9−0.3 at $v_{\rm LSR} = +76$ km s^{-1}, and G23.5−0.0 at $v_{\rm LSR} = +91$ km s^{-1} (Downes et al. 1980). They have excitation parameters U of 120 pc cm^{-2} and 150 pc cm^{-2}, respectively. Both are on the far side of the Galactic plane at the extension of the Scutum arm in the spiral pattern proposed by Georgelin & Georgelin (1976). If GW 23.0−1.6+100 is associated with these H II regions, then the distance to this object is more likely ~ 10 kpc and the length of the structure would be almost 1.4 kpc.

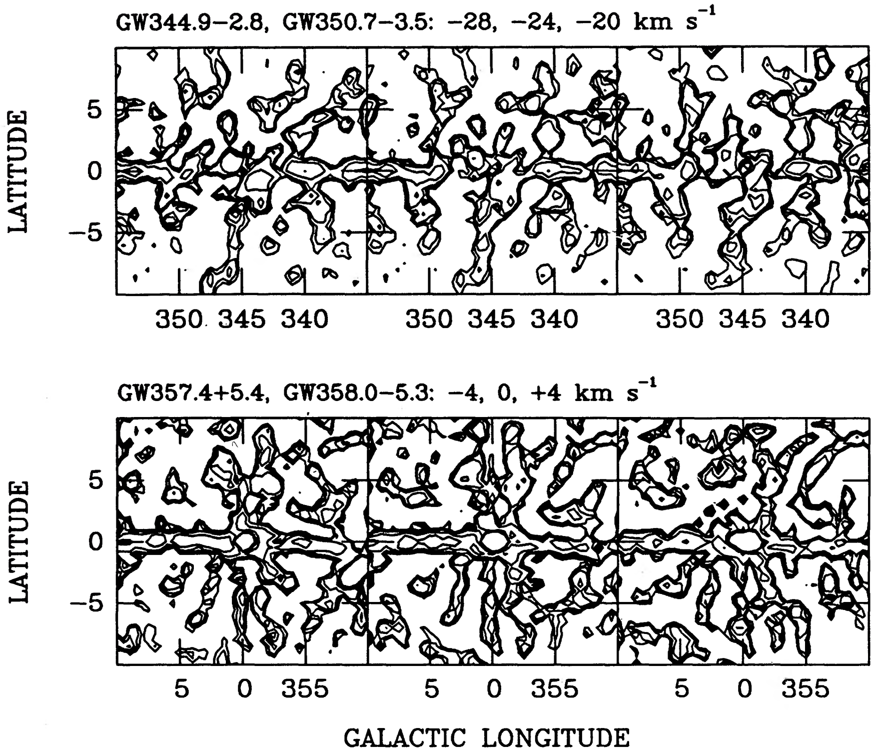

FIG. 13—*Continued*

GW 23.0−1.6+60 is vertical to the plane and forms a closed loop around $l = 25°$ between $v_{\rm LSR} = +60$ and $+68$ km s^{-1} (see channel maps for GW 35.8−2.2 in Fig. 13). It is very interesting to see a corresponding loop structure at $b > 0°$ between $v_{\rm LSR} = +52$ and $+60$ km s^{-1} because there is a very bright, $U = 210$ pc cm^{-2}, radio H II region G25.4−0.2 at $v_{\rm LSR} = +59$ km s^{-1} (Downes et al. 1980). It is located on the far side of the Galactic plane at the extension of the Sagittarius arm. If the H I structure is associated with this H II region, then the distance to this object is ∼11 kpc and its height above the plane is ∼800 pc.

5.3. *GW 31.6−5.9*

This is an object at the tangential point of the Scutum arm, and it is not clear whether this is a single structure or is a result of two distinct structures overlapped by chance. Between $v_{\rm LSR} = +68$ to $+104$ km s^{-1}, it appears as a very prominent and persistent structure at $l = 30°5$ (Fig. 13). Between $v_{\rm LSR} = +56$ to $+64$ km s^{-1}, on the other hand, the structure is centered at $l = 31°2$ (see channel maps of GW 35.8−2.2 in Fig. 13). The shift in position occurs rather abruptly, and we consider them as two distinct objects: GW 31.6−5.9+88 and GW 31.6−5.9+60. The H II regions S66 and S69, listed in Table 5, have a rest velocity near ∼ +50 km s^{-1} (Fich et al. 1990), and they are probably not associated with GW 31.6−5.9+88.

Instead, GW 31.6−5.9+88 is very likely to be associated with either one, or both, of two giant radio H II regions in this region: G29.9−0.0 at $v_{\rm LSR} = +98.5$ km s^{-1} and G30.8−0.0 (W43) at $v_{\rm LSR} = +90$ km s^{-1} (Downes et al. 1980). They have excitation parameters U of 150 pc cm^{-2} and 200 pc cm^{-2}, respectively. The relatively strong, $T_b \sim 6$ K, 408 MHz continuum emission associated with this structure is likely to be the thermal emission.

5.4. *GW 35.8−2.2*

This is a long, ∼9° (470 pc at $d = 3$ kpc) vertical structure between $v_{\rm LSR} = +52$ and $+68$ km s^{-1} (Fig. 13). Below 52 km s^{-1}, the structure is not clearly defined. There is a Sharpless H II region right on GW 35.8−2.2; S72 at $(l, b, v_{\rm LSR}) = (36°4, -1°7, +62$ km s^{-1}). Its relatively high-b position and the agreement both in position and in radial velocity almost certainly indicates that the H II region S72 is physically associated with GW 35.8−2.2.

There are also radio H II regions at somewhat different velocities, $v_{\rm LSR} \simeq 45$ km s^{-1}, near $l = 35°$: G35.1−1.5, G35.2−1.8, and G35.3−1.8 (Downes et al. 1980). The strong 408 MHz emission listed in Table 3 as being associated with GW 35.8−2.2 is located at $l = 35°$ and is likely to be the thermal emission associated with these H II regions. The association of these H II regions with GW 35.8−2.2 and/or the other vertical structure at $l = 34°$ should be examined.

5.5. *GW 46.4+5.5*

This is also a long, ∼9° (360 pc at $d = 2.3$ kpc) vertical structure between $v_{\rm LSR} = +28$ and $+40$ km s^{-1} (Fig. 13). A unique thing for this structure is its associated 408 MHz emission, only a small fraction of which is due to the small, ∼12′, H II region S78 at $(l, b, v_{\rm LSR}) = (46.8, +3.9, +42$ km s^{-1}). The 408 MHz emission is present along the worm's whole structure, generally at a slightly smaller (∼0°5) Galactic longitude. This shift between the radio continuum emission and the H I emission is similar to what we observe in the North Polar Spur (Borken & Iwan 1977; Heiles et al. 1980). If we are looking at a case similar to the North Polar Spur, then the 408 MHz emission is mostly non-thermal and the energy source might be at a smaller Galactic longitude.

1992ApJ...390..108K

5.6. *GW 331.3−4.3*

GW 331.3−4.3 is a vertical structure appearing between $v_{\rm LSR} = -100$ and -76 km s^{-1} (Fig. 13). This line of sight crosses the tangential point of the Norma arm, and GW 331.3−4.3 is probably in the Norma arm. There is a group of H II regions at $(l, v_{\rm LSR}) = (331^\circ.7, -87$ km s$^{-1})$ (group 1 of Georgelin & Georgelin 1976), and the association of these H II regions with GW 331.3−4.3 needs to be examined.

5.7. *GW 340.0+4.8*

This vertical structure starts to appear at $v_{\rm LSR} = -60$ km s^{-1} and persists to $v_{\rm LSR} = 0$ km s^{-1}. The position, however, suddenly shifts from $l = 340.5$ to $l = 340.0$ near $v_{\rm LSR} = -40$ km s^{-1}, and it is possible that the structure is a result of two or more overlapping structures. Here we consider only the structure between $v_{\rm LSR} = -60$ km s^{-1} and -44 km s^{-1}. It is interesting enough to note that there appears another vertical structure at $l = 343^\circ$ parallel to GW 340.0+4.8 in the same velocity range (Fig. 13). The two are possibly associated with each other. There is a very large, $\sim 5^\circ$, H II region RCW 113 centered at $(l, b) = (342^\circ.7, +1^\circ.8)$ (Rodgers et al. 1960). The radial velocity of this H II region measured at $(l, b) = (342^\circ.8, +0^\circ.0)$ is -24 km s^{-1} according to Geogelin & Georgelin (1976). However, since the H II region is large and considerably shifted to the upper region, it is not clear whether the measured velocity at the plane represents the systematic velocity of RCW 113. The association of RCW 113, GW 340.0+4.8, and the enhanced 408 MHz emission along the structure should be examined.

5.8. *GW 344.9−2.8 and GW 350.7−3.5*

These two long vertical structures appear between $v_{\rm LSR} = -32$ and -8 km s^{-1} (Fig. 13). Although it is not listed in Table 3, there seems to be enhanced 408 MHz emission associated with GW 350.7−3.5. The 408 MHz emission is slightly, $\sim 0^\circ.5$, shifted to smaller l.

5.9. *GW 357.4+5.4, GW 358.0−5.3, and GW 0.5−5.9*

These three structures, appearing around $v_{\rm LSR} = 0$ km s^{-1}, are lying in a direction toward the Galactic center (Fig. 13), and the distances to them are very uncertain. The association of these structures with the activity near the Galactic center remains to be examined. GW 358.0−5.3 and GW 0.5−5.9 have 408 MHz emission along their structures.

6. DISCUSSION

What are the 118 structures cataloged in Table 2? And also the 35 structures in Table 3? The vertical structures in radio continuum emission, called "radio spurs," have been known since the detection of the prominent North Polar Spur in the earliest days of radio astronomy (see Salter & Brown 1988). Sofue (1988), for example, applied a background-removal technique to the 408 MHz whole-sky map of Haslam et al. and found numerous radio spurs, which are generally much larger and at higher Galactic latitudes than ours. (Between $l = 330^\circ$ and $l = 30^\circ$, for example, structures with $|b|$ less than 5° cannot be identified in his filtered map.) Sofue concluded that most spurs in the inner Galaxy ($320^\circ < l < 40^\circ$) are located at $R_G < 5$ kpc, based on the local (-10 km s$^{-1} < v_{\rm LSR} < +10$ km s^{-1}) H I distribution being smooth in contrast to the radio continuum distribution. He further claimed that the radio spurs do not seem to have a definite correlation with H I emission features. We can interpret the radio spurs detected by Sofue, and also the North Polar Spur, as objects that are similar to our worm candidates but which are much closer than our worm candidates. We would have missed Sofue's spurs because they are so large that our filter would have rejected them and because our technique emphasized objects at low Galactic latitude. The point here is that there are numerous vertical structures in the Galaxy, particularly inside the solar circle, and that the structures detected either by us or by previous people mainly in radio continuum emission are biased samples of these structures, samples whose properties are limited by the selection technique.

The above, of course, does not answer the fundamental question, namely the origin of those vertical structures. It is not likely that they all have a common origin: Some structures have both H I and 408 MHz emission, whereas the others have only either one of the two. The 408 MHz emission in some structures is probably nonthermal as in the North Polar Spur. It is "common wisdom" that the 408 MHz emission is mostly, if not all, nonthermal, and indeed, in Figure 1, we can easily identify well-known supernova remnants such as the Cygnus loop at $(l, b) = (74^\circ.0, -8^\circ.5)$ or the Crab at $(l, b) = (184^\circ.6, -5^\circ.8)$. However, these supernova remnants do not necessarily have corresponding 100 μm emission, whereas the 35 structures listed in Table 3 appear both in infrared and 408 MHz continuum. (Broadbent, Haslam, & Osborne 1989 separated the 408 MHz emission into thermal and nonthermal components by cross-correlating the 408 MHz survey of Haslam et al. with the *IRAS* 60 μm map.) Our results (Fig. 12) suggest that the 408 MHz emission in those structures that have associated H II regions is likely to be thermal. In GW 17.8+3.0, which is one of those with an associated H II region, we already know from Müller, Reif, & Reich (1987) that it is a thermal spur rising vertically from the H II region S54, which is located at 100 pc above the Galactic plane. The origin of each entry in our tables—and indeed, the reality and significance of each entry—can be found only by studying it in detail.

One possible interpretation of these vertical structures, which might apply at least for some of the objects in this paper, is that they are the walls surrounding a superbubble produced by a combined action of stellar winds and supernova explosions in an OB association. This is almost certainly the case for the North Polar Spur, which is believed to have been driven by six to 10 supernova explosions in the Sco-Cen association (see Koo & McKee 1992 for a discussion). The 35 cataloged structures in Table 3 are similar to the North Polar Spur in the sense that they have both H I and 408 MHz emission: $\sim 70\%$ of them are possibly associated with H II regions. Whether the 408 MHz emission is thermal or nonthermal might depend not only on the age of the superbubble but also on the brightness of the central OB association, which decreases with time as the stars die off. Hence, the entries in Table 3, particularly the ones discussed in § 5, are the prime candidates for the ionized walls surrounding superbubbles.

It has been known that one of the major components of the interstellar medium is the "warm ionized medium (WIM)" (Mezger 1978; Kulkarni & Heiles 1988; Reynolds 1989, 1991). Its detailed spatial distribution is not clear, but several observations suggest that it is clumped and widespread throughout the Galactic disk (Anantharmaiah 1985, 1986; Lockman 1980) and is extended to $\gtrsim 1$ kpc (scale height of the volume averaged electron density $\langle n_e \rangle$) above the Galactic plane. Although it has been realized that the only source which can supply enough ionizing radiation is O stars, it is not clear how the UV photons can escape from H II regions to maintain the widespread diffuse WIM, particularly at $\gtrsim 1$ kpc above the Galactic plane. (Kulkarni & Heiles 1988; Cox 1989).

We now propose that the WIM is very likely the ionized gas associated with the worms (see also Heiles 1991). As discussed in the above, our results suggest that some worms have associated ionized gas, which is possibly the ionized inner surface of a supershell. The inner surface of a supershell is likely to be ionized by the ionizing photons from the central OB association because the interior of a supershell is relatively free of neutral gas. The vertical extent of the ionized gas in this picture will be a few times the scale height (~ 190 pc) of the thin gaseous disk, at which the supershell breaks out due to the Rayleigh-Taylor instability. This vertical extent of 400–600 pc is comparable to the exponential scale height ~ 430 pc of the ionized gas derived from the observed vertical distribution of the volume-averaged $\langle n_e \rangle$ and $\langle n_e^2 \rangle$ (Kulkarni & Heiles 1988).

In addition to the inner surface of supershells, the gas far from the Galactic plane but located right above large superbubbles might be ionized. After the break-out, the supershell evolves to a cylindrical shell with the top portion "transparent" for UV photons except for the blocking due to some dense fragments of the shell. Hence, some fraction of the UV photons $f_{\rm UV}$ from the central OB association can directly ionize the gas outside the thin disk. The fraction $f_{\rm UV}$ can be estimated from the results of numerical simulations. For a cylindrical bubble of radius R_b, the fraction of the solid angle occupied by the top portion is $1 - (Z_b/R_b)/[1 + (Z_b/R_b)^2]^{1/2}$, where Z_b is the height of the cylinder above the plane. (We consider only the upper or the lower half of the plane.) According to the numerical results of Mac Low et al. (1989), the ratio Z_b/R_b seems to be between 1 and 2. Therefore, the fraction of UV photons that can be used to ionize the gas outside the thin disk is

$$f_{\rm UV} \sim f_{\rm block}\left[1 - \frac{Z_b/R_b}{\sqrt{1 + (Z_b/R_b)^2}}\right] \sim 0.1 , \qquad (5)$$

where $f_{\rm block}$ is a numerical factor to account for the blocking due to the dense fragments and we arbitrarily set $f_{\rm block} = \frac{1}{2}$. Using the factor $f_{\rm UV}$ and the average Lyman continuum photon flux $F_{\rm UV} = 2.8 \times 10^{50}$ photons kpc^{-2} s^{-1} in the Solar neighborhood (Abott 1982), we may estimate the emission measure perpendicular to the Galactic plane, $\mathrm{EM}_\perp$, due to the WIM far from the plane:

$$\mathrm{EM}_\perp \sim \frac{f_{\rm UV} F_{\rm UV}}{2\alpha_B} \sim 1.0 \ \mathrm{cm}^{-6} \ \mathrm{pc} . \qquad (6)$$

The factor 2 in the denominator of equation (6) accounts for the fact that half of the photon flux goes upward and the other half goes downward. This $\mathrm{EM}_\perp$ is about half of the observed value ~ 2 cm^{-6} pc in the solar neighborhood (Reynolds 1984, 1991; Kulkarni & Heiles 1988). (We used $T_e = 5000$ K to convert the Hα intensity to the EM.) The other half of the observed $\mathrm{EM}_\perp$ may be contributed by the WIM relatively close ($|z| < 400$–600 pc) to the plane, which is possibly the ionized walls of superbubbles.

Hence, although a detailed study on the spatial correlation between the WIM and the worm is needed, the above discussions seem to support the possibility that the UV photons from O stars not only ionized the inner surfaces of supershells but also escape vertically through the holes surrounded by the worms to ionize the gas outside the thin disk.

If the worms are really the walls surrounding superbubbles which are filled with hot gas, then the distribution of the worms should tell us about the filling factor of the hot ionized gas. In a preliminary report (Koo et al. 1990), we derived a *lower* limit of ~ 0.1 for the filling factor of hot gas by counting only those structures that appear to be vertical. The total mass injection rate to the halo by superbubbles was estimated to be greater than $\sim 0.2 \ M_\odot \ \mathrm{yr}^{-1}$. Regarding the incompleteness of our search and the uncertain origin of cataloged structures, however, we want to postpone another estimation of these parameters to the future.

7. SUMMARY

The goal of this paper was to generate a catalog of candidates for the worms that are possibly the walls surrounding the superbubbles. We have identified 118 isolated structures that appear both in H I and in infrared (60 and 100 μm). Properties of the objects in our catalog are biased by the algorithm used to define the objects, so our catalog is not complete. Among 118 structures, 35 appear also in the radio continuum (408 MHz). Whether or not these structures are associated with superbubbles needs further study. We found that 70% of the 35 structures possibly have associated H II regions, and they have a higher probability for the association with superbubbles. Some well-defined individual candidates are described in § 5.

The study of physical properties of these structures by cross-correlating maps at different wavebands is limited by different resolutions, different beam shapes, and different sensitivities. However, it is shown that the data in Table 2 can still be used to derive some useful statistical properties: (1) there is a systematic increase of the 100 μm emissivity, $I_{100}/N_{\rm H\,I}$, toward the Galactic interior, which is consistent with the increase of the general ISRF. (2) The 100 μm emissivity of the structures associated with H II regions, 7.1 ± 2.2 MJy sr^{-1}/10^{20} cm^{-2}, is considerably larger than 3.1 ± 0.9 MJy sr^{-1}/10^{20} cm^{-2} for the structures without associated H II regions. (3) The average 60–100 μm intensity ratio of all structures is large, 0.28 ± 0.03, which may indicate that the grains associated with atomic gas have a relatively large population of small grains. (4) There is a good correlation between the 408 MHz brightness temperature and the 60 μm intensity of those structures associated with H II regions. For bright structures, the correlation seems to be consistent with what we would expect for a diffuse H II region, which indicates that the associated 408 MHz emission is very likely thermal. On the other hand, the faint structures are generally brighter at 408 MHz than what we would expect, which may indicate that the 408 MHz emission of these faint sources is mostly nonthermal, as in the North Polar Spur.

For some worm candidates that are associated with H II regions, the observed correlation between the IR and 408 MHz radio emission possibly originates from the ionized walls of superbubbles by the same OB associations that create the H II regions. The interior of a supershell is relatively free of neutral gas, which allows UV photons to reach the shell walls (which are the worms) and to ionize the inner surface of the walls. In addition, the relatively open tops of large supershells should allow the warm ionized gas far from the galactic plane to be ionized by the UV photons from O stars escaping through vertical holes above superbubbles.

We thank the staff of the NASA Space Science Data Center (NASA/GSFC) for providing the data from the *Infrared Astronomical Satellite* and the catalog of Blitz et al. (1982) in a machine-readable form. This research has made use of the SIMBAD data base, operated at CDS, Strasbourg, France. This work was supported in part by NSF grant AST-8818544 to Carl Heiles. B. C. K. wishes to thank the Center for Astrophysics for its financial support.

REFERENCES

Abbott, D. C. 1982, ApJ, 263, 723
Allen, R. J., Goss, W. M., & van Woerden, H. 1973, A&A, 29, 447
Allen, R. J., van der Hulst, J. M., Goss, W. M., & Huchtmeier, W. 1978, A&A, 64, 359
Anantharamaiah, K. R. 1985, J. Astroph. Astron., 6, 203
———. 1986, J. Astrophy. Astron., 7, 131
Beichman, C. A. 1987, ARA&A, 25, 521
Beuermann, K., Kanback, G., & Berkhuijsen, E. M. 1985, A&A, 153, 17
Blitz, L., Fich, M., & Stark, A. A. 1982, ApJS, 49, 183
Bloemen, J. B. G. M., Deul, E. R., & Thaddeus, P. 1990, A&A, 233, 437
Borken, R. J., & Iwan, D. C. 1977, ApJ, 218, 511
Boulanger, F., & Pérault, M. 1988, ApJ, 330, 964
Brinks, E., & Bajaja, E. 1986, ApJ, 169, 14
Broadbent, A., Haslam, C. G. T., & Osborne, J. L. 1989, MNRAS, 237, 381
Burton, W. B. 1988, in Galactic and Extragalactic Astronomy, ed. G. L. Verschuur & K. I. Kellermann (New York: Springer), 295
Cox, D. P. 1989, in IAU Colloq. 120, Structure and Dynamics of the Interstellar Medium, ed. G. Tenorio-Tagle, M. Moles, & J. Melnick (New York: Springer), 500
Désert, F. X., Bazell, D., & Boulanger, F. 1988, ApJ, 334, 815
Désert, F. X., Boulanger, F., & Puget 1990, A&A, 237, 215
Deul, E. R., & den Hartog, 1990, A&A, 229, 362
Downes, D., Wilson, T. L., Bieging, J., & Wink, J. 1980, A&AS, 40, 379
Draine, B. T., & Anderson, N. 1985, ApJ, 292, 494
Fich, M., Treffers, R. R., & Dahl, G. P. 1990, AJ, 99, 622
Georgelin, Y. M., & Georgelin, Y. P. 1976, A&A, 49, 57
Haslam, C. G. T., Salter, C. J., Stofell, H., & Wilson, W. E. 1982, A&AS, 47, 1
Heiles, C. 1984, ApJS, 55, 585
———. 1990, 354, 483
———. 1991, in Evolution of Interstellar Matter & Dynamics of Galaxies
Heiles, C., Chu., Y.-H., Reynolds, R. J., Yegingil, I., & Troland, T. H. 1980, ApJ, 242, 533
Heiles, C., Reach, W. T., & Koo, B.-C. 1988, ApJ, 332, 313
Humphreys, R. M. 1978, ApJS, 38, 309
IRAS Catalog & Atlases: Explanatory Supplement 1988, ed. C. A. Beichman, G. Neugebauer, H. J. Habing, P. E. Clegg, & T. J. Chester (Washington, DC: US GPO)
IRAS Zodiacal Observation History File (version 3). 1988, as described in the *IRAS* Explanatory Supplement 1988
Kamphuis, J., Sancisi, R., & van der Hulst, T. 1991, A&A, 244, L29
Kerr, F. J., Bowers, P. F., Jackson, P. D., & Kerr, M. 1986, A&AS, 66, 373
Koo, B.-C., Heiles, C., & Reach, W. T. 1991, in IAU Symp. 144, The Interstellar Disk-Halo Connection in Galaxies, ed. H. Bloemen (Dordrecht: Kluwer Academic), 165
Koo, B.-C., & McKee, C. F. 1992, ApJ, , in press
Kulkarni, S. R., & Heiles, C. 1988, in Galactic and Extragalactic Astronomy, ed. G. L. Verschuur, & K. I. Kellermann (New York: Springer), 95
Lockman, F. J. 1980, in Radio Recombination Lines, ed. P. A. Shaver (Dordrecht: Reidel), 185
Mac Low, M.-M., & McCray, R. 1988, ApJ, 324, 776
Mac Low, M., McCray, R., & Norman, M. L. 1989, ApJ, 337, 141
Marálková, P. 1974, Ap&SS, 27, 3
Mathis, J. S., Mezger, P. G., & Panagia, N. 1983, A&A, 128, 212
Mathis, J. S., Rumpl, W., & Nordsieck, K. H. 1977, ApJ, 217, 425
Mezger, P. G. 1978, A&A, 70, 565
Müller, P., Reif, K., & Reich, W. 1987, A&A, 183, 327
Osterbrock, D. E. 1989, Astrophysics of Gaseous, Nebulae and Active Galactic Nuclei (Mill Valley, CA: University Science Books)
Reynolds, R. J. 1989, ApJ, 339, L29
———. 1991, ApJ, 372, L17
Rodgers, A. W., Campbell, C. T., & Whiteoak, F. B. 1960, MNRAS, 121, 103
Salter, C. J., & Brown, R. L. 1988, in Galactic and Extragalactic Astronomy, ed. G. L. Verschuur & K. I. Kellermann (New York: Springer), 1
Sharpless, S. 1959, ApJS, 4, 257
Sofue, Y. 1988, PASJ, 40, 567
Tenorio-Tagle, G., Bodenheimer, P., & Różyczka, M. 1987, A&A, 182, 120
Tomisaka, K. 1990, ApJ, in press
Tomisaka, K., & Ikeuchi, S. 1986, PASJ, 38, 697
Weaver, H., & Williams, D. R. W. 1973, A&AS, 8, 1
Wilson, T. L., Mezgar, P. G., Gardner, F. F., & Milne, D. K. 1970, A&A, 6, 364